Scattering Center Extraction and Recognition Based on ESPRIT Algorithm

Master's thesis (Tech.)
University of Turku
Department of Information Technology
2022
Yaru Wang

Supervisors:
Dr. Paavo Nevalainen
Assoc. Prof. Tomi Westerlund

UNIVERSITY OF TURKU
Department of Information Technology

WANG YARU: Scattering Center Extraction and Recognition Based on ESPRIT Algorithm
Master of Science in Technology Thesis, 63 p.
Computer Systems
July 2022

Inverse Synthetic Aperture Radar (ISAR) generates high quality radar images even in low visibility. And it provides important physical features for space target recognition and location. This thesis focuses on ISAR rapid imaging, scattering center information extraction, and target classification.

- Based on the principle of Fourier imaging, the backscattering field of radar target is obtained by physical optics (PO) algorithm, and the relation between scattering field and objective function is deduced. According to the resolution formula, the incident parameters of electromagnetic wave are set reasonably. The interpolation method is used to realize three-dimensional (3D) simulation of aircraft target, and the results are compared with direct imaging results.
- CLEAN algorithm extracts scattering center information effectively. But due to the limitation of resolution parameters, traditional imaging can't meet the actual demand. Therefore, the super-resolution Estimation of Signal Parameters via Rotational Invariance Techniques (ESPRIT) algorithm is used to obtain spatial target location information. The signal subspace and noise subspace are orthogonal to each other. By combining spatial smoothing method with ESPRIT algorithm, the physical characteristics of geometric target scattering center are obtained accurately. In particular, the proposed method is validated on complex 3D aircraft targets and it proves that this method is applied to most scattering mechanisms.
- The distribution of scattering centers reflects the geometric information of the target. Therefore, the electromagnetic image to be recognized and ESPRIT image are matched by the domain matching method. And the classification results under different radii are obtained. In addition, because the neural network can extract rich image features, the improved ALEX network is used to classify and recognize target data processed by ESPRIT. It proves that ESPRIT algorithm can be used to expand the existing datasets and prepare for future identification of targets in real environments. Final a visual classification system is constructed to visually display the results.

Keywords: Synthetic aperture radar; scattering center; ESPRIT; super resolution; radar target recognition

Content

Chapter 1 Introduction

1. 1 Research background and motivation

Due to the continuous evolution of signal processing technology, the radar image is becoming more and more refined. When the incident frequency is high frequency, the scattering target is equivalent to the distribution of multiple independent scattering centers, and the target energy is approximately the energy sum of scattering centers. During radar imaging, the geometric parameters of scattering center represent the structural information of radar target. ISAR [1] acquires the spatial distribution of scattering centers and obtains structural characteristics such as orientation, shape and size.

Multi-dimensional imaging and imaging refinement are two major requirements for ISAR development. Radar imaging is gradually expanded from one-dimensional (1D) to 3D. The 1D image is like the vector sum projected on the radar ray by the target scattering center echoes obtained by wideband radar signal. The distance between scattering center and the radar is projected onto 1D plane. On this basis, two-dimensional (2D) image is obtained by adding azimuth feature. It is of great significance for the development of target recognition. The 2D distribution of the target is obtained by the relative movement and the signal transmitted broadband. However, both 1D image and 2D images are affected by the attitude of the target and limited by the resolution [2]. To solve this problem, pitch information is added and objects display in 3D space. By improving the pitching resolution, the height information is obtained without being affected by the attitude of the object.

High resolution means rich target characteristics. The traditional Range-Doppler (RD) method achieves high resolution by increasing the synthetic aperture time and signal bandwidth. However, RD algorithm has the following limitations. Firstly, it needs to put forward higher requirements for the system. The imaging time of non-cooperative targets is limited and the data acquisition is passive. Secondly, when the imaging angle is too large, scattering centers will produce large distance migration. It causes image distortion and resolution reduction [3]. Therefore, researchers begin to consider super-resolution algorithms. The essence of this algorithm is signal processing. Compared with the fuzzy image obtained by Fourier method at low resolution, super-resolution algorithm obtains fine images without limiting resolution parameters and increasing imaging accumulation time. Multi-signal Classification (MUSIC) [4] and ESPRIT [14] are both iconic methods. Compared with MUSIC, ESPRIT does not need to search spectrum peaks one by one, and it greatly reduces the complexity. For the ESPRIT method, radar signals are calculated by eigen decomposition of covariance matrix. It breaks the Rayleigh limit and makes the mean square error of parameter estimates to approach the Cramér–Rao bound. This method has good parameter estimation ability and is of great significance for automatic recognition of ISAR images in the future.

1. 2 Progress in research at home and abroad

1.2.1 Inverse synthetic aperture radar imaging technology

Wiley first proposed the concept of Synthetic Aperture Radar (SAR) in 1951. In 1957, Willow Run laboratory at the University of Michigan obtained the world's first SAR image. The concept of ISAR imaging was basically put forward at the same time as SAR. In the early 1960s, Willow Run Laboratory proposed RD technology [5-6]. And it successfully realized the imaging of space orbit targets. This marks that the development of ISAR imaging technology has entered the stage of practical application. Subsequently, Westinghouse successfully achieved tracking and ISAR imaging of space orbiting targets. In 1970, Lincoln Laboratory of Massachusetts Institute of Technology developed the world's first long-range high resolution broadband imaging radar and it called DARPA-Lincoln C-Band Observables Radar. ISAR images of low-Earth space orbit targets like satellites were obtained [7-8]. Chen and Andrews et al. carried out research on ISAR imaging of aircraft targets by ground-based radar in 1978. According to the characteristics of the radar system, ISAR imaging processing was divided into translational compensation and RD imaging. The translational compensation was divided into envelope compensation and phase compensation, and the corresponding processing methods were proposed [9-10]. In the early 1980s, ISAR images of non-cooperative maritime ship targets were obtained by The US Naval Laboratory and Texas Instruments [11]. In terms of imaging algorithm, Chen proposed the range-instantaneous doppler algorithm and adopted the joint time-frequency transform technology to solve the imaging problem of complex moving targets [12-13]. It indicated that the ISAR algorithm and system research have entered the stage of rapid development.

The earliest research of radar imaging technology in China began in 1986. Beihang University began to build electromagnetic scaling models for targets like aircraft. And they carried out relevant measurements of electromagnetic scaling ratio and scientific experiments of turntable imaging. The 23rd Institute of the 2nd Aerospace Academy successfully developed China's first long-range imaging radar with 400 MHz bandwidth in 1993. Three years later, due to the implementation of the "Ninth Five-Year Plan" electronic pre-research plan, the Key Laboratory of Radar Signal Processing of Xidian University carried out researches on real-time radar imaging. Researchers systematically studied translational compensation and maneuvering target imaging principle. The 23rd Institute of the 2nd Aerospace Academy successfully extended the working bandwidth of ground observation radar to 800 MHz in 2006. In 2008, the working bandwidth of the all-polarization ground imaging radar was extended to 1 GHz by the 14th Institute of China Light and Power Group. ISAR imaging technology is developing continuously in our country, but there is still a certain gap with foreign technology.

1.2.2 Super resolution imaging algorithm

High resolution means high image quality. In the early 1990s, a large number of super-resolution algorithms were proposed for ISAR imaging. The classical subspace algorithm MUSIC was first proposed by Schmidt et al. in 1979 [4]. The principle was to use matrix eigenspace decomposition. Based on the orthogonal property of signal subspace and noise subspace, spatial spectral function was constructed to find spectral peak. Parameter estimation performance was superior. But this method needed to search spectral peaks one by one and stored the array flow matrix, thus it caused heavy computation. To solve this problem, ESPRIT algorithm was proposed by Roy et al in 1986 [14]. According to the subspace rotation invariance of the received data, signal parameters were directly calculated by the generalized eigenvalues of autocorrelation matrix. Compared with MUSIC, it had better robustness and lower operation complexity. TLS-ESPRIT algorithm was proposed later and it improved the performance of spectrum estimation by increasing part of calculation. Mathews et al published UCA-ESPRIT in 1994 and Zoltowski et al proposed 2D U-ESPRIT algorithms in 1996. These methods were applicable to uniform circular arrays [15] and realized automatic pairing of azimuth and elevation estimation. In order to accurately obtain 2D Direction-of-Arriva (DOA) estimation and the incident wave frequency, 3D Unitary ESPRIT was proposed by Haardt et al in 1997[16]. In 1999, Liu et al published the virtual 2D ESPRIT algorithm [17]. It had the advantages of lower requirements for signal sub-array, small computation and high accuracy. However, this method only estimated a small number of scattering centers at the same time. In 2005, Feng et al used 1D unitary ESPRIT algorithm to obtain high resolution ISAR images [18], but this algorithm only applied super-resolution technology in one direction. In 2013, the single-shot 2D ESPRIT algorithm was proposed by Wang et al [19]. An equivalent covariance matrix was constructed through the data generated by a single shot in this algorithm. In 2016, Liu et al proposed an extended ESPRIT based on dynamic phase compensation technology. ESPRIT was extended as an alternative method for the DOA estimation of arbitrary arrays except for MUSIC [20]. Zhang et al applied convex optimization algorithm to spectrum estimation in 2020 [21]. The anti-noise performance of traditional LS-ESPRIT algorithm was improved, and the higher resolution was taken into account.

1. 3 Main content of the thesis research

This thesis is mainly divided into three parts. Fast ISAR imaging, scattering centers extraction by ESPRIT algorithm, and image classification.

The main research contents are as follows:

The relation between electromagnetic field data by PO method and imaging function is deduced. The traditional Fourier interpolation method is used to reconstruct objects in 3D space, and the results of direct imaging are compared.

High resolution ISAR images are obtained based on 3D ESPRIT algorithm. The ESPRIT algorithm is extended from one dimension to three dimensions. Meanwhile the results are compared with Fourier imaging in all dimensions. In particular, we use complex aircraft models to validate the algorithm and ESPRIT is applicable to most scattering mechanisms. The comparison results of ESPRIT algorithm and CLEAN algorithm under 2D condition are given. The results show ESPRIT has the advantages of high precision, high resolution and strong robustness to noise. Reconstructed images provide important features for the automatic target recognition of SAR.

Then SAR target recognition based on neighborhood matching method is proposed. 2D ESPRIT obtains the characteristics of scattering centers. The neighborhood matching method is used to match the reconstructed image and ESPRIT image, and the type of target is judged by similarity. In addition, the dataset is obtained by ESPRIT method and the improved ALEX network is used to extract image features. The recognition rate of aircraft target simulation images reaches 99.22%, and the recognition rate of mixed data also reaches 99.39%. The generated database is conducive to the aircraft recognition in future. And the aircraft target classification system is established to display the classification results visually.

1. 4 Chapters arrangement of the thesis

This thesis studies the process from radar data imaging to SAR image recognition. This thesis consists of five chapters, and contents are arranged as follows.

In the first chapter, the background and significance of the research are introduced.

Current situation of ISAR imaging algorithm and super-resolution imaging algorithm are investigated.

The second chapter begins with SAR imaging model. Imaging principle is analyzed and resolution formula is deduced. At the same time, the traditional Fourier transform imaging is extended to from one dimension to three dimensions. The radon transform is used to project 3D image to three dimensions.

In the third chapter, the CLEAN algorithm is used to extract scattering centers from 2D aircraft images first. Then the super-resolution algorithm ESPRIT is introduced. Simulation results in 1D, 2D and 3D cases are given. Under the same parameter settings, the processed results of CLEAN algorithm and ESPRIT algorithm are given. Simulation results show that ESPRIT provides specific physical information for each scattering center and is not bound by resolution parameters. By changing the parameters, the electromagnetic characteristics are easily obtained at various angles. This method provides a dataset for subsequent identification.

The fourth chapter mainly introduces radar target recognition methods. Using neighborhood matching method to recognize 2D target electromagnetic image. The target is identified according to the matching degree of scattering centers. Besides, the improved ALEX network is used to classify and recognize the scattering images generated by ESPRIT. Besides, the aircraft target classification system is constructed to display the classification results intuitively.

In the fifth chapter, the summary and prospect of this thesis.

Chapter 2 ISAR Imaging Principle

2. 1 Introduction

ISAR achieves high quality imaging of some long-range non-cooperative objects like missiles. The imaging principle is that the radar decomposes the target motion direction to form a virtual synthetic array and uses the large aperture of the synthetic array to improve the resolution. Therefore, the formation of ISAR array is influenced by the change of target's heading, speed, attitude and other factors. For target recognition, 3D objects contain much more information than 2D images. Therefore, it is necessary to study ISAR 3D imaging technology.

2. 2 ISAR imaging model

During ISAR imaging, the radar does not move while the observed target moves. The target displacement is divided into radial displacement and transverse displacement. Azimuth direction refers to the direction perpendicular to the track in the surveying belt, and range direction refers to the direction along the radar in the surveying belt. On the plane's 2D turntable, the azimuth direction and the range direction are perpendicular to each other.

The movement of the target relative to the radar is equivalent to the motion of the turntable. ISAR imaging can be built on a 2D turntable imaging model, as shown in Figure 2.1. Assuming that the target is moving uniformly, the relative motion between the target and the radar is divided into rotational component and translational component. We suppose object has a reference point. Target translation means that the reference point moves along the target trajectory, and the overall attitude of the target relative to the radar remains unchanged. The rotation variable means that the point on the target rotates around the reference point [22].

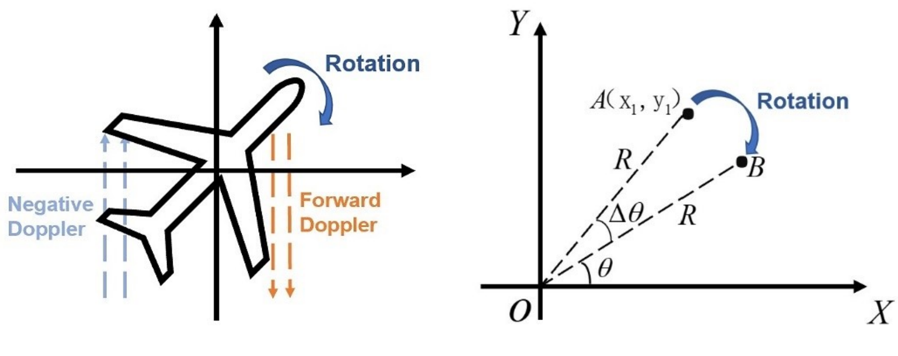

(a) (b)

Figure 2.1 ISAR turntable imaging model. (a)Target rotation model, (b) Point target trajectory

2.2.1 Resolution

Resolution is an important parameter to measure image quality. Range resolution represents the minimum distance to distinguish two targets in the same azimuth. High resolution depends on whether radar transmits wideband signals. Azimuth resolution refers to the ability to distinguish the minimum azimuth difference between two targets at the same distance. It depends on the velocity of scattering centers and is obtained by calculating the doppler resolution. The Figure 2.2 shows a schematic of range resolution and azimuth resolution in 2D imaging [23].

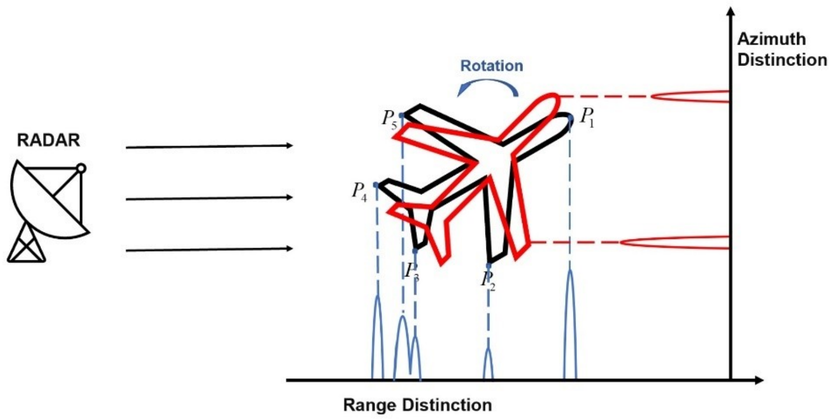

Figure 2.2 Range distinction and azimuth distinction diagram

The distance between the radar and each scattering center is different. Therefore, each scattering center reflects the echo signal with different time. Positions of scattering centers are distinguished by time delay, and it's called range resolution. The range resolution represents the different distance information of scattering centers on the target.

We suppose the radar sends a pulse signal, and signal is defined as [23]:

$$S_t'(t,t') = \cos(2\pi c f_0 t') \tag{2.1}$$

where,

$$-\frac{T'}{2} \le \left|t' - t\right| \frac{T'}{2}$$

t' represents time, t represents pulse center, T' represents pulse width and f_0 represents carrier frequency. We assume that the radar sends rectangular envelope pulses with constant amplitude. For ease of understanding, the constant amplitude and phase are ignored. Then the echo signal is:

$$S_t(t,t') = \sigma \cos[2\pi f_0 (t' - \frac{2r(t)}{c})] \tag{2.2}$$

where,

$$-\frac{T'}{2} \le t' - t - \frac{2r(t)}{c} \le \frac{T'}{2}$$

In formula 2.2, σ represents the scattering coefficient of scattering centers, c represents the speed of light, and $r(t)$ represents the distance between different scattering centers and radar.

Let $\tau = t' - t$, τ is the delay relative to t. The above formula is expressed as:

$$S_t(t,t') = \sigma \cos[2\pi f_0 (t' - \frac{2r(t)}{c})] \tag{2.3}$$

where,

$$\left|\tau - \frac{2r(t)}{c}\right| \le \frac{T'}{2}$$

In formula 2.3, τ is fast time and t is slow time. We can see that the echo pulses of scattering centers at different distances are centered on different values τ. Thus, scattering centers at different distances are distinguished by different time delays.

The range resolution ρ_r is inversely proportional to the signal bandwidth B. The formula is:

$$\rho_r = \frac{cT'}{2} = \frac{c}{2B} \tag{2.4}$$

According to the above formula, the range resolution is determined by the signal bandwidth. The larger the bandwidth, the higher the resolution.

As shown in Figure 2.1(a), when the target moves clockwise, each scattering center has different velocity and this corresponds to different doppler values. The line between the center and the radar is called the axis. The scattering centers on the axis have no radial motion relative to the radar, so the doppler frequency is 0. Scattering centers on both sides of the axis have positive doppler value or negative doppler value. The farther away from the axis, the greater the doppler value of scattering centers. By Fourier transform, echoes of different range units are converted to doppler domain. The transverse distribution of the target is obtained by distinguishing different doppler values.

In Figure 2.1(b), in the time interval between two radar signals, the rotation angle of the target is $\delta\theta$. One of the scattering centers rotates from P to P_1, then the longitudinal displacement is:

$$\begin{aligned} \triangle y_p &= r_p \sin(\theta - \delta\theta) - r_p \sin(\theta) \\ &= -x_p \sin\delta\theta - y_p(1 - \cos(\delta\theta)) \end{aligned} \tag{2.5}$$

Where, the coordinate of P is (x_p, y_p), and $x_p = r_p \cos\theta, y_p = r_p \sin\theta$. The phase change of sub-echo caused by longitudinal displacement $\triangle y_p$ is:

$$\begin{aligned} \triangle\varphi_p &= -\frac{4\pi}{\lambda}\triangle y_p \\ &= -\frac{4\pi}{\lambda}[-x_p \sin\delta\theta - y_p(1 - \cos(\delta\theta))] \end{aligned} \tag{2.6}$$

When $\delta\theta$ is very small, $\sin\delta\theta \approx \delta\theta$ and $\cos\delta\theta \approx 1$. Then the formula changes to:

$$\triangle\varphi_p = \frac{4\pi}{\lambda} x_p \delta\theta \tag{2.7}$$

Through the analysis of the above equation, we conclude that the phase difference

$\vartriangle\varphi_p$ of the two observed target echoes is proportional to the transverse distance x_p. There is a phase difference $\exp(j\frac{4\pi}{\lambda}x_p\delta\theta)$ between the two echoes, and the phase change is shown as doppler change. The larger the x_p, the larger the doppler frequency value of this scattering center. It shows that the echo doppler values of scattering centers at different transverse distances are not the same, and it provides the conditions to distinguish these scattering centers.

We assume that M echoes are received in the imaging process, then the total rotation angle is $\vartriangle\theta = M\delta\theta$. The transverse distance difference of two scattering centers is supposed as $\vartriangle x$, thus the total phase difference of their echoes is:

$$\vartriangle\phi_M = \frac{4\pi}{\lambda}\vartriangle\theta\vartriangle x \tag{2.8}$$

Fourier transform is used as doppler analysis. if $\vartriangle\phi_M \geq 2\pi$, two points are distinguished. So, the azimuth resolution ρ_a is:

$$\rho_a = \frac{\lambda}{2\Delta\theta} \tag{2.9}$$

In formula 2.9, The azimuth resolution is inversely proportional to the angle difference. And 2D images are obtained by Fourier transform twice.

2. 3 Conventional interpolated Fourier imaging

The point of the PO method [24-25] is the integral formula of Stratton-Chu scattering field. The PO method determines the surface induced current of the target according to the incident field. The scattering field is represented by the integral of the induced current, and it simplifies the calculation process of the scattering field. This method divides the target surface into several surface elements, and these elements are equivalent to the ideal smooth plane. The current of the target surface is equal to the sum of the current of the surface elements in the illuminated area. Final the scattering field is obtained. The PO method is based on three assumptions [26-28]:

(1) The induced current on the surface of the scatterer is only determined by the

region which is directly irradiated by the incident electromagnetic wave. And the induced current only exists in the illuminated area. The induced current of each surface element is independent of each other and there is no current continuity.

(2) Far-field approximation. The radius of curvature on the surface of the object is larger than the wavelength of incident wave, and the scatterer is electrically large.

(3) Tangent plane approximation. The current distribution at the plane is equal to the current distribution at the infinite tangent plane.

The first hypothesis is true if the second hypothesis is true.

Therefore, the scattering field $E^{(s)}(r)$ expression of PO method is directly set as the current integration of the illuminated area on the surface of the object [24]:

$$E^{(s)}(r)=\frac{-ikZ_0e^{ikr}}{4\pi r}\hat{\boldsymbol{r}}\times\hat{\boldsymbol{r}}\times\int_{S_{lit}}dS(r')J_{\mathrm{PO}}(r')e^{ik\hat{\boldsymbol{r}}\cdot r'} \tag{2.10}$$

Where, S_{lit} represents the illuminated area of the scatterer surface, k represents the wave number, and Z_0 represents the wave impedance of free space. r is the position vector of the observation point, and it includes the amplitude coefficient r and the unit direction $\hat{\boldsymbol{r}}$. r' is the position vector of any point located on the illuminated area S_{lit}. $\hat{\boldsymbol{n}}(r')$ is the surface normal vector. The surface induced current J_{PO} is written as:

$$J_{\mathrm{PO}}(r')=2\hat{\boldsymbol{n}}(r')\times H^{(i)}(r') \tag{2.11}$$

We substitute $H^{(i)}(r')=\frac{1}{Z_0}\hat{\boldsymbol{r}}_i\times E^{(i)}$ into the scattering field formula and obtain the expression:

$$E^{(s)}(r)=\frac{-ikZ_0e^{ikr}}{2\pi r}\hat{\boldsymbol{r}}\times\hat{\boldsymbol{r}}\times\int_{S_{lit}}\left(\hat{\boldsymbol{n}}(r')\times\hat{\boldsymbol{r}}_i\times E^{(i)}\right)dS(r')e^{ik(\hat{r}_i-\hat{r})\cdot r'} \tag{2.12}$$

Setting the direction of electric field polarization as $\hat{\boldsymbol{p}}$. The following scalar scattering field E_p expression is obtained:

$$E_p = \hat{\boldsymbol{p}} \cdot E^{(s)}(r) = \frac{-ikZ_0 e^{ikr}}{2\pi r} \int_{S_{lit}} \hat{\boldsymbol{p}} \cdot \left[\hat{\boldsymbol{r}} \times \hat{\boldsymbol{r}} \times \left(\hat{\boldsymbol{n}}(r') \times \hat{\boldsymbol{r}}_i \times E^{(i)} \right) \right] dS(r') e^{ik(\hat{\boldsymbol{r}}_i - \hat{\boldsymbol{r}}) \cdot r'} \quad (2.13)$$

Since global scattering is the sum of surface element scattering, the integrand is the target function $O(r')$:

$$O(r') = \hat{\boldsymbol{p}} \cdot \left[\hat{\boldsymbol{r}} \times \hat{\boldsymbol{r}} \times \left(\hat{\boldsymbol{n}}(r') \times \hat{\boldsymbol{r}}_i \times E^{(i)} \right) \right] \delta\left(S(r') \right) \quad (2.14)$$

Where, $\delta\left(S(r')\right)$ is the impulse function. It is used to express whether the plane element is in the bright region S_{lit}. That is:

$$S(r') \begin{cases} = 0, r' \in S_{lit} \\ \neq 0, r' \notin S_{lit} \end{cases} \quad (2.15)$$

Then the scattering field formula is obtained：

$$E_p = \hat{\boldsymbol{p}} \cdot E^{(s)}(r) = \frac{-ikZ_0 e^{ikr}}{2\pi r} \int_{S_{lit}} O(\mathbf{r}') dS(\mathbf{r}') e^{ik(\hat{\boldsymbol{r}}_i - \hat{\boldsymbol{r}}) \cdot r'} \quad (2.16)$$

Let the vector $k = k\left(\hat{\boldsymbol{r}} - \hat{\boldsymbol{r}}_i\right)$, the above equation is expressed as

$$E_p(k) = \frac{-ikZ_0 e^{ikr}}{2\pi r} \iiint_{S_{lit}} O(r') e^{-i\boldsymbol{k} \cdot r'} d^3 r' \quad (2.17)$$

We can see that the scattering field $E_p(k)$ collected in the wavenumber domain is the 3D Fourier transform form of the objective function $O(r')$. Therefore, after obtaining the scattering field $E_p(k)$, the estimation $\tilde{O}(r')$ of the objective function $O(\mathbf{r}')$ is obtained through the inverse Fourier transform. And $k = \hat{x}k_x + \hat{y}k_y + \hat{z}k_z, r' = \hat{x}x' + \hat{y}y' + \hat{z}z'$ is substituted：

$$\tilde{O}(x', y', z') = \frac{1}{(2\pi)^3} \iiint \frac{2\pi r}{-ikZ_0 e^{ikr}} \hat{\boldsymbol{p}} \cdot E^{(s)}(k, \theta, \varphi) e^{i\left(k_x x' + k_y y' + k_z z'\right)} dk_x dk_y dk_z \quad (2.18)$$

It is the objective function estimation of ISAR imaging.

Traditional ISAR imaging is to sample backscattering field $E^{(s)}$ in multi-frequency and multi-angle. Then the inverse Fourier transform is applied to the scattering matrix in wavenumber field to obtain the image. For ISAR image $I(x, y, z)$, we assume that the frequency f, azimuth φ and pitching angle θ. Sampling matrix of the scattering field is $E^s(k,\varphi,\theta)$ and $k=\omega/c$. The imaging formula is as follows:

$$I(x,y,z)=FT^{-1}\{FT^{-1}\{FT^{-1}\left[E^s(k,\varphi,\theta)\right]\}\} \tag{2.19}$$

Since the Fast Fourier Transform (FFT) has to be performed on uniform data, interpolation of the scattering field matrix is required.

2.3.1 Two-dimensional interpolation imaging

In Figure 2.3, the original electromagnetic field data is obtained by uniform sampling in frequency-angle domain. But when it is converted to wavenumber domain, it becomes non-uniform data.

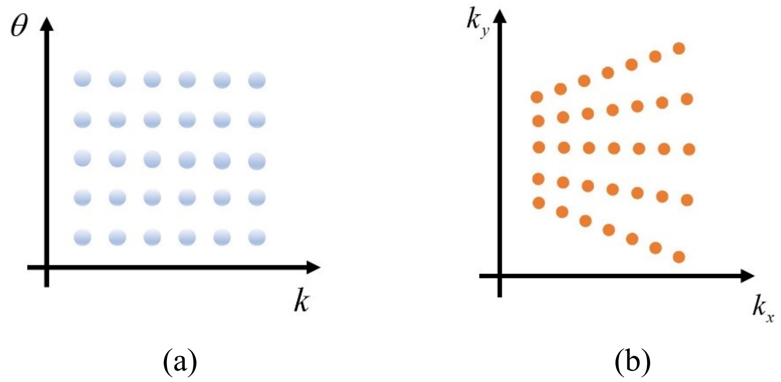

Figure 2.3 2D scattering field sampling. (a) $k-\theta$ field uniformly sampled (b) k_x-k_y field nonuniform sampling

The prerequisite of Fourier imaging is that electromagnetic field data is uniform. Thus, the traditional interpolation method is to interpolate the scattered field data $E^s(k,\theta)$ and divide the uniform grid in the corresponding coordinate k_x-k_y. Then mapping the divided uniform grid back to the field $k-\theta$. After interpolation, the uniform scattered field $E^s(k_x,k_z)$ is obtained in k_x-k_y coordinate system. Then FFT imaging is performed.

The nearest neighbor interpolation, bilinear interpolation and interpolation of natural adjacent points are commonly methods to interpolate scattered field data. Their principle is to estimate the pixel value by using the information weight of the nearby points to be interpolated. Principles of three interpolation methods are described below [29].

(1) Nearest neighbor interpolation

Nearest interpolation is to find the point closest to the unknown point and directly assign the value to the interpolated point.

The coordinates of the four pixels around the interpolation point $S(x+u, y+u)$ are supposed as (x, y)、$(x+1, y)$、$(x+1, y+1)$、$(x, y+1)$ respectively. Distances between the point S and the four pixels are d_1, d_2, d_3, d_4 respectively. Then the pixel values of the point S is shown in the formula:

$$f(x+u, y+u) = f_i(x, y) \tag{2.20}$$

Where, i represents the minimum distance under the condition $i / d_j = \min(d_j, j=1,2,3,4)$. The result of nearest neighbor interpolation is shown in Figure 2.4.

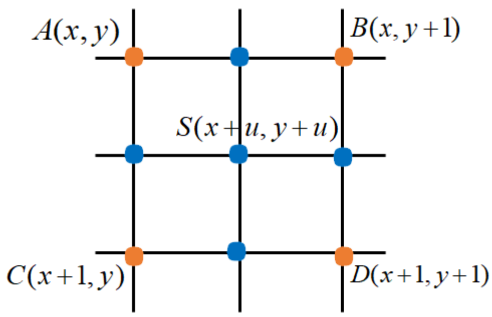

Figure 2.4 Nearest field interpolation

Nearest neighbor interpolation algorithm is simple and the calculation time is short. However, its disadvantages are that the interpolation effect is not ideal and it is easy to cause blocking effect and sawtooth phenomenon.

(2) Bilinear interpolation

Instead of using only one point value, the principle of bilinear interpolation algorithm is to linearly weighted the pixel values of the four points adjacent to the unknown pixel points and assign the final value to the point to be interpolated. Compared with the previous method, this method improves the block effect to a certain extent.

The coordinates of the four points around the interpolation point $S(x+u, y+u)$ are respectively supposed as (x,y)、$(x+1,y)$、$(x+1,y+1)$、$(x,y+1)$. Then the pixel values of the interpolation point are:

$$f(x+u, y+u) = m_1 f(x,y) + m_2 f(x,y+1) + m_3 f(x+1,y) + m_4 f(x+1,y+1) \qquad (2.21)$$

In this formula, m_1, m_2, m_3, m_4 respectively represent the weight coefficients of four known points. As shown in the figure below, the pixel values of point A and point B are calculated by linear weighting of the pixel values of four known points respectively.

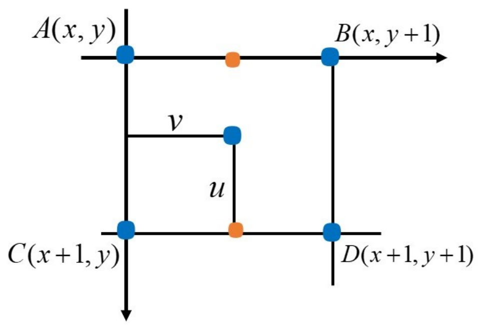

Figure 2.5 Bilinear Interpolation

(3) Interpolation of natural adjacent points

The principle of this method is based on a set of Thiessen polygons. When a new data point is added to the data set, the Tyson polygons are modified. And the average weight of the adjacent points is used to determine the weight of the points to be interpolated. And it is proportional to the target Tyson polygon. At the same time, the natural adjacent interpolation method does not extrapolate isolines at the convex positions of the data points, such as the contours of the Tyson polygon.

For 1D case, we use the sphere model to verify the accuracy of the algorithm. 1D simulation of three spheres has been considered. The positions are 0m, 2m and 4m respectively. The azimuth is 60°. The frequency range is from 9.7 GHz to 10.3 GHz, with 128 points. Results are as follows. We can see that the positions of the three spheres are accurate and prominent.

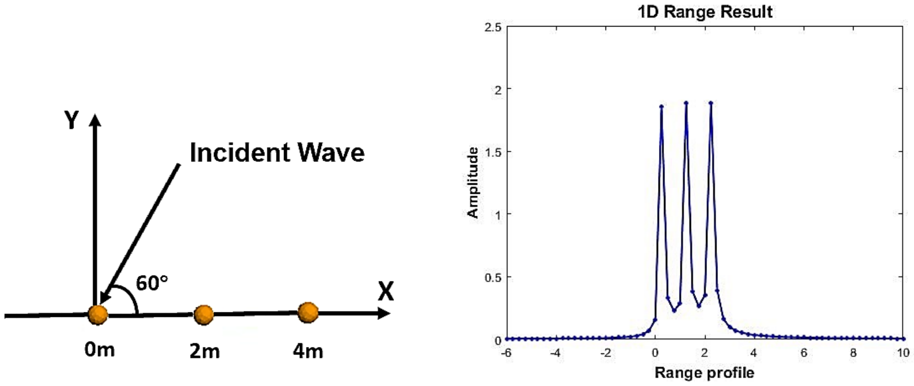

(a) (b)

Figure 2.6 1D FFT imaging. (a) Spheres model, (b) 1D Range result

For 2D case, aircraft with 10m*4m*0.7m in Figure 2.6 is simulated. Parameters are: Frequency range is from 9.7 GHz to 10.3 GHz; azimuth angles are from -1.5° to 1.5°; and sampling numbers are 128*128.

The imaging results are shown in Figure 2.7:

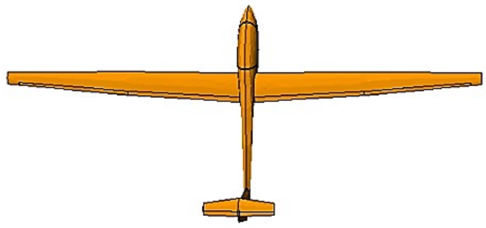

(a)

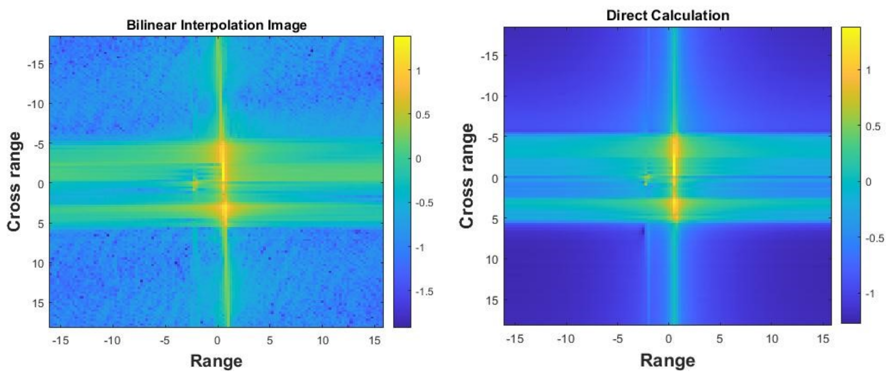

(b) (c)

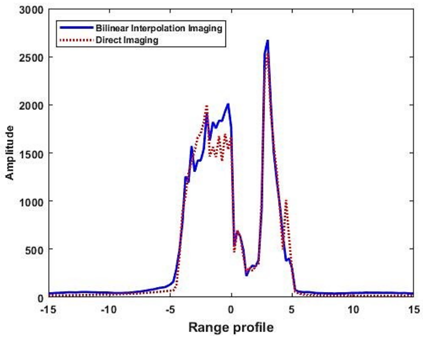

(d)

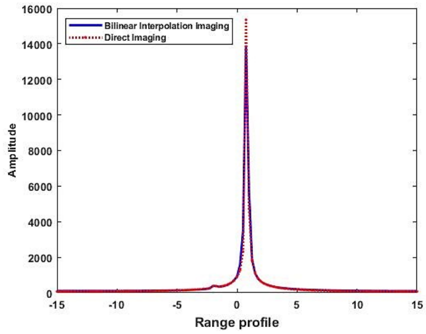

(e)

Figure 2.7 2D imaging. (a) Aircraft Model, (b) Bilinear interpolation imaging, (c) Direct imaging, (d) 1D distance image profile comparison, (e) 1D azimuth image profile comparison

The running time of FFT imaging is 0.22s, while the running time of direct interpolation is 3.46s. The calculation time of fast interpolation is much less than that of direct calculation. Both images show characteristics of the aircraft well, but the generated images still have many sidelobes. Therefore, adding window function to filter the signal. If the signal is directly truncated with rectangular window, frequency leakage will occur. Therefore, non-rectangular window is added to improve frequency leakage. Generally, hamming window greatly attenuates the image sidelobe, and the peak attenuations of the main lobe and the first lobe reach 40dB. The Hamming window equation is defined as [30]:

$$w(n) = a_0 - (1-a_0)\cdot\cos(\frac{2\pi n}{N-1}), \quad 0 \le \mathrm{n} \le \mathrm{N\text{-}1} \tag{2.22}$$

where,

$$a_0 = 0.53836$$

Adding hamming window to the above 2D images. In Figure 2.8, we can see that energy reduction and the sidelobe of the image is much less.

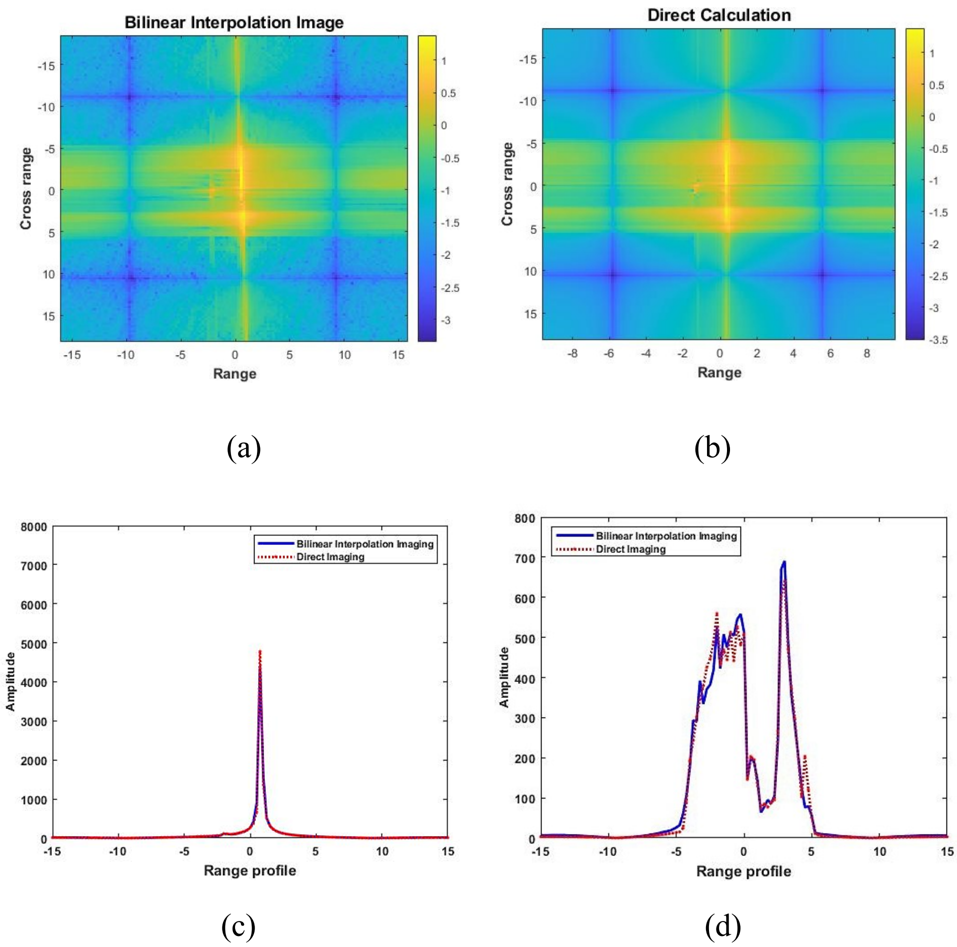

Figure 2.8 Image with hamming window. (a) Bilinear interpolation imaging, (b) Direct imaging, (c) 1D distance image profile comparison, (d) 1D azimuth image profile comparison

2.3.2 Three-dimensional interpolation imaging

Compared with the 2D images, 3D images increase the resolution in pitch angle and obtain the spatial height information of each scattering center. Similarly, 3D electromagnetic field data also needs uniform interpolation, and the interpolation model is shown in Figure 2.9:

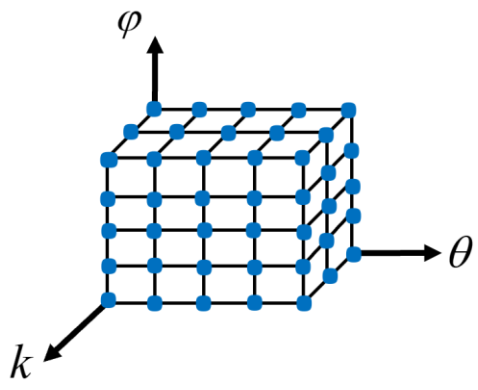

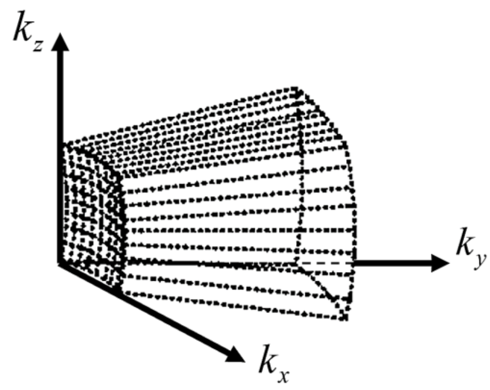

Figure 2.9 3D scattering field sampling. (a) $k-\theta-\varphi$ field uniformly sampled (b) $k_x-k_y-k_z$ field nonuniform sampling

In projection-patch theory, the common 2D image is generated by the projection superposition of the 3D image on a certain plane, while the 1D direction is generated by the projection superposition of the 2D image on the azimuth. Radon transform is used to reduce dimension [31-32], and the formula is:

$$O_{proj}=\int_{-\infty}^{\infty} o\ d_{\rho} \tag{2.23}$$

In formula 2.23, ρ is the integral path. In general, radar images contain distance direction. In the operation from 2D image to 1D range image, ρ is perpendicular to the range direction. And in the dimensionality reduction operation from 3D image to 2D image, ρ is perpendicular to the imaging plane. We introduce the 3D discrete radon transform:

$$O_{proj}=\sum_{l=0}^{L-1}\sum_{m=0}^{M-1}\sum_{n=0}^{N-1} o(l,m,n)\delta[\rho-m\cos(90^{\circ}+\chi)-n\sin(90^{\circ}+\chi)] \tag{2.24}$$

Where, $\chi\in[0^{\circ},180^{\circ})$ is the dip angle of the image plane. And it is superimposed along a straight line $\rho{=}m\cos(90^{\circ}+\chi){+}n\sin(90^{\circ}+\chi)$. When $\rho{=}0^{\circ}$, the projected image is the most common radar imaging situation, frequency-azimuth scanning 2D image. When $\rho{=}90^{\circ}$, the projected image is a frequency-pitch scanning 2D image. When ρ takes an arbitrary value, it means that vertical and distance scans follow this direction. Therefore, we obtain 2D images under different poses through the projection of 3D images on different planes.

In order to verify the feasibility of ISAR 3D imaging technology based on Fourier transform, we conduct a simulation experiment. Aircraft is 3m*1.1m*0.2m, frequency center is 10 GHz, the bandwidth is 1.5 GHz, the azimuth sampling range is -4.31° to 4.31°, the elevation angle range is 80.69° to 89.31°, and the total number of samples is 60*60*60. Figure 2.10 is the results of interpolation imaging. And Figure 2.11 is the results of direct imaging.

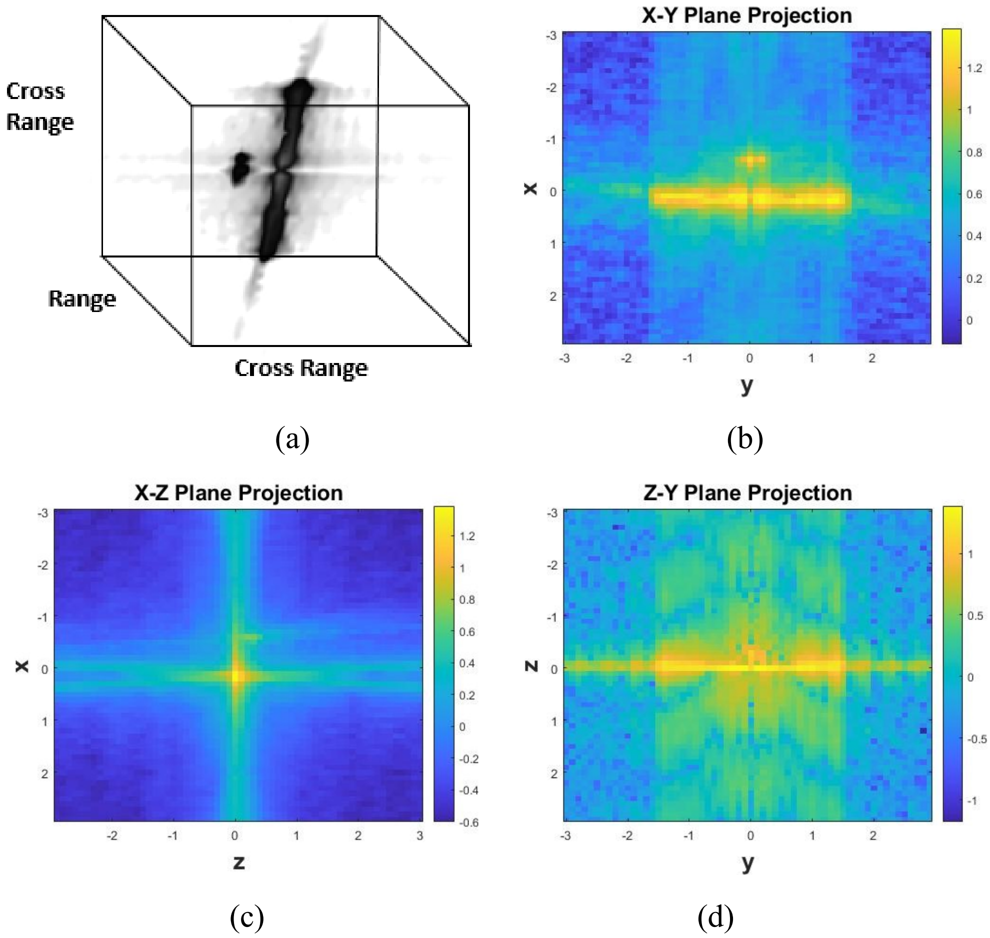

Figure 2.10 3D interpolation imaging. (a) 3D spatial imaging, (b) X-Y plane projection, (c) X-Z plane projection, (d) Z-Y plane project

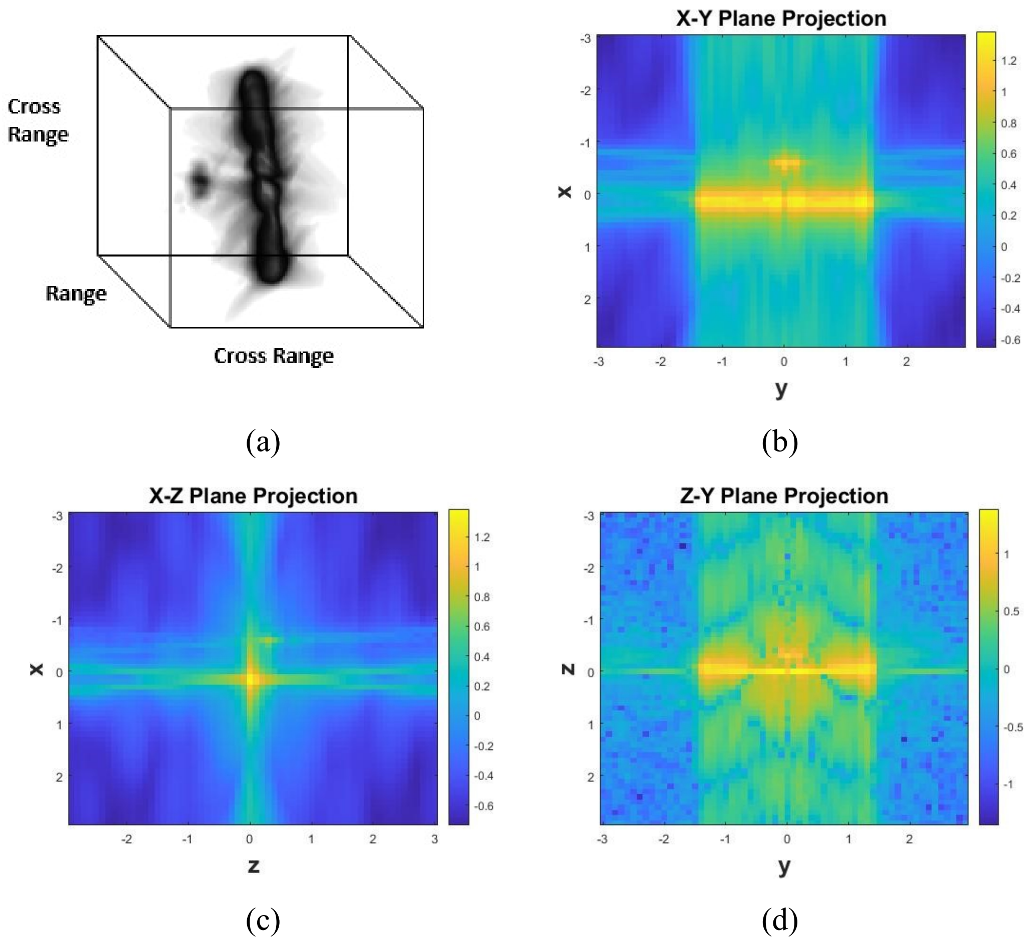

Figure 2.11 3D direct imaging. (a) 3D spatial imaging, (b) X-Y plane projection, (c) X-Z plane projection, (d) Z-Y plane projection

Both methods accurately reconstruct the plane's 3D structure. The difference is that the time of Fourier rapid imaging is 351.77s less than that of direct imaging and it improves calculation speed.

2. 4 Conclusion

This chapter describes the principle of radar imaging first, and deduces the formula of azimuth resolution and range resolution. Then, the scattering field formula is derived by PO method. The relation between scattering field and 3D target imaging function is deduced. The interpolation method is introduced to realize the conversion from non-uniform data to uniform data. According to the simulation method, the 2D Fourier imaging and 3D Fourier imaging of the aircraft model are successfully realized. The corresponding direct imaging results are also given for comparison.

Chapter 3 3D Scattering Center Extraction Based on ESPRIT Algorithm

According to high frequency scattering theory, when the target size is very large relative to the radar transmitting signal wavelength, the scattering echo of the target is equivalent to the coherent synthesis result of multiple independent strong scattering sources. These strong scattering sources are usually referred to as scattering centers. Radar target recognition is mainly to identify unknown targets by analyzing the backscattering field of the target. Extracting the characteristic parameters of these scattering centers and establishing a reasonable scattering center model is always a research hotspot in the field of radar target reconstruction.

In general, FFT imaging is a convenient method to obtain target images. Classical CLEAN algorithm is used to extract scattering center of the image, and it is computationally effective. But the resolution is limited by radar parameters settings like bandwidth and center frequency. The scattering centers parameters are determined within the Fourier resolution unit. Then various high-resolution algorithms are proposed to solve this problem. Among them, MUSIC algorithm and the ESPRIT are the most prominent. But MUSIC algorithm requires exhaustive search spectrum and it is time consuming. ESPRIT algorithm uses the characteristic structure of autocorrelation matrix to obtain the signal eigenvalue. And it extracts scattering center locations by phase delay information. Therefore, ESPRIT algorithm does not require a search process and is efficient [33].

3. 1 CLEAN algorithm

3.1.1 Principle

In the early 1990s, Ling et al proposed the CLEAN method of ray tracing to extract the scattering centers in ISAR images [34] and used the extracted scattering center information to reconstruct ISAR images. CLEAN is an iterative deconvolution image processing algorithm with high robustness, as well as a fast greedy search algorithm. The deconvolution process of image is the inverse of the convolution process. The location and amplitude of the scattering center are extracted from the given convolution image. In the mth iteration, the point with the current highest amplitude is found. Its position and amplitude are recorded as (x_m, y_m) and A_m respectively. A new ISAR image is obtained by subtracting this point contribution from the current image. Then continuing to search for the next peak value. The iterative process is simplified as follows:

$$I_R^{(m+1)} = I_R^{(m)} - \gamma A_m h\left(x - x_m, y - y_m\right) \tag{3.1}$$

Where, $I_R^{(m)}$ is the image at mth iteration, and γ is the parameter controlling the stability of iteration and $0 < \gamma < 1$ [35]. In the process of iteration, the energy of the original image has been decaying so as to ensure good convergence. There are three common convergence criteria for iteration:

(1) The ratio of the remaining image energy to the original image is less than a certain value. The value usually is 10%.

(2) The number of scattering centers reaches the theoretical maximum estimation.

(3) The amplitude of the scattering center is lower than the theoretical minimum.

We end up with a series of scattering centers $\left(A_1\left(x_1, z_1\right), A_2\left(x_2, z_2\right), \ldots, A_M\left(x_M, z_M\right)\right)$ as an equivalent model to the target. To some extent, the number of scattering centers represents the sparsity of the ISAR images.

3.1.2 Results

F35 aircraft model is simulated. Parameters are: Frequency is from 9.5 GHz to 10.5 GHz; azimuth angle is from -2.87° to 2.87°; and sampling numbers are 128*128. In Figure 3.1, taking 90%, 70% and 50% energy to reconstruct the image respectively.

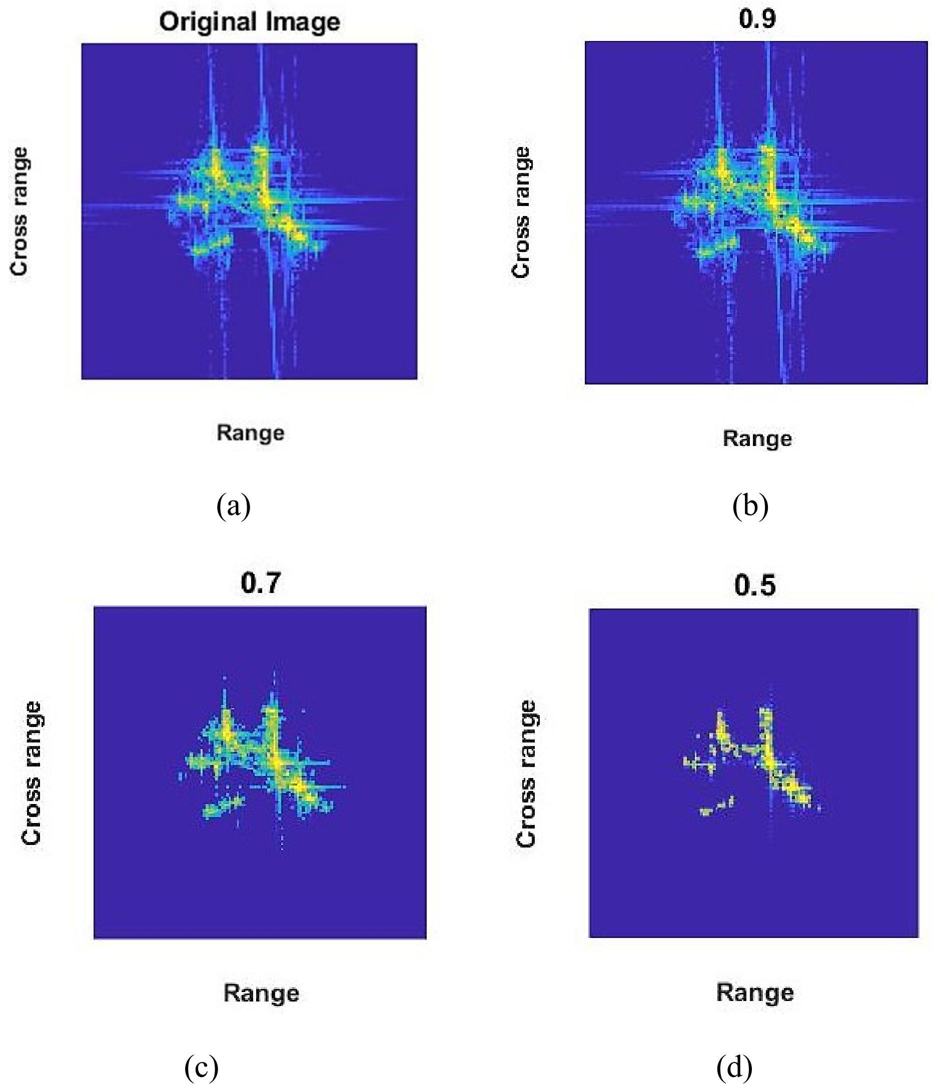

Figure 3.1 CLEAN image. (a) FFT Image, (b) 90% energy reconstruction, (c) 70% energy reconstruction, (d) 50% energy reconstruction

We can see the main features of the aircraft target have been preserved. But the CLEAN algorithm still requires FFT image as input, this algorithm is affected by image resolution. And the ray tracing method is not applicable to the signal collected by the frequency conversion radar. Therefore, the super-resolution algorithm based on ESPRIT is proposed.

3. 2 Three-dimensional ESPRIT algorithm

3.2.1 Three-dimensional signal model

In high frequency, the target backward electromagnetic field information is equivalent to the information sum of N scattering centers [36]. When the transmitted incident wave is incident on the target at the frequency f_n, the echo signal is defined as [37]:

$$X(n) = \sum_{k=1}^{N} r_{\mathrm{k}} \exp(j2\pi f_n t_k) + w(n) \tag{3.2}$$

The initial frequency of transmission wave is f_0, the frequency step is Δf and there are N frequencies. Then the echo signal is expressed as:

$$\begin{aligned} X(n) &= \sum_{k=1}^{N} r_{\mathrm{k}} \exp(j2\pi(f_0 + n\Delta f)t_k) + w(n) \\ &= \sum_{k=1}^{N} [r_{\mathrm{k}} \exp(j2\pi(f_0)t_k)] \exp(j2\pi n\Delta f t_k) + w(n) \end{aligned} \tag{3.3}$$

Let B_k replaces $A_{\mathrm{k}} \exp(j2\pi f_0 t_k)$ and P_k replaces $\exp(j2\pi n\Delta f t_k)$. We get the general form of signal:

$$X(n) = \sum_{k=1}^{N} B_{\mathrm{k}} P_k + w = PB + w \tag{3.4}$$

Where, $X = [\mathrm{x}_1 \ \mathrm{x}_2 \ ... \ \mathrm{x}_{Ns}]$ is the array matrix receiving matrix, $P = [p_1 \ p_2 \ ... \ p_{Ns}] = [1 \ \exp(2\Pi\Delta f t_k) \ ... \ \exp(2\Pi(N_s - 1)\Delta f t_k)]$ and $B = [b_1 \ b_2 \ ... \ b_{Ns}]^T$ are the signal data matrix. $w = [w_1 \ w_2 \ ... \ w_{Ns}]^T$ is the noise matrix.

For the 3D situation, the target motion is decomposed into three mutually orthogonal dimensions. The coordinate of the kth scattering center is set as $(x_{\mathrm{k}}, y_{\mathrm{k}}, z_{\mathrm{k}})$. When the incident frequency is f, the array element echo is stated as:

$$X(f,\beta,\gamma) = \sum_{k=1}^{N} A_k \exp(j\frac{4\Pi}{c} f(x_k \cos\beta\cos\gamma + y_k \sin\beta\sin\gamma + z_k \sin\gamma)) + w(n) \tag{3.5}$$

A_k represents reflection parameter, $d_k = x_k \cos\beta\cos\gamma + y_k \sin\beta\sin\gamma + z_k \sin\gamma$ represents distance between scattering center and the origin, β represents azimuth angle, γ means pitching angle, and $w(n)$ means zero-mean Gaussian white noise.

Since the data under all attitude angles cannot be processed, the data need to be discretized in three directions first. The frequency sampling point is N_f, then $f_{n1} = [f_0\ f_1\ \dots f_{N_f-1}]$. The number of azimuth sampling is N_β, then $\beta_{n2} = [\beta_0\ \beta_1\ \dots\ \beta_{N_\beta-1}]$. The number of pitch angles is N_γ, then $\gamma_{n3} = [\gamma_0\ \gamma_1\ \dots\ \gamma_{N_\gamma-1}]$.

After discretely sampling, data is transformed to cartesian coordinate system for data reconstruction. The discrete non-uniform data is transformed into uniform data by interpolation method described in chapter 2 in wavenumber field. As shown in Figure 3.2:

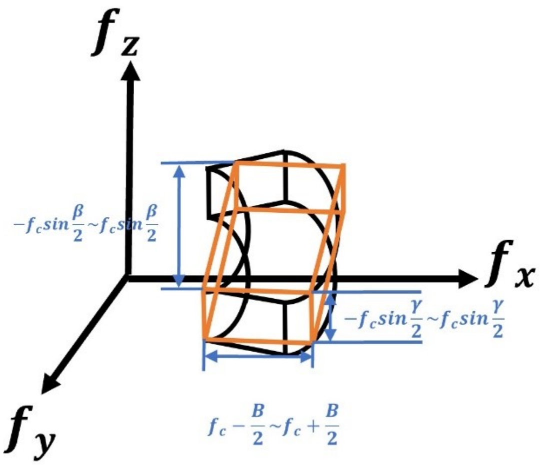

Figure 3.2 Reformatting radar data

After data resampling and uniform interpolation, the signal becomes:

$$X(n_1, n_2, n_3) = \sum_{k=1}^{N} A_k \exp(j\frac{4\Pi}{c}(f_{n_1}^x x_k + f_{n_2}^y y_k + f_{n3}^z z_k)) + w(n_1, n_2, n_3) \tag{3.6}$$

where,

$$f_{n_1}^x = f\cos\beta\cos\gamma,\ f_{n2}^y = f\sin\beta\sin\gamma,\ f_{n3}^z = f\sin\gamma$$

3.2.2 Three-dimensional ESPRIT method based on spatial smoothing

High-resolution method focuses on the analysis of the signal autocorrelation matrix. When the autocorrelation matrix is full rank, the scattering centers are separated accurately. Spatial smoothing method is used to eliminate the influence between different scattering centers. And increasing the number of observations does not affect the rank. The basic form of spatial smoothing method is as follows [38-39]:

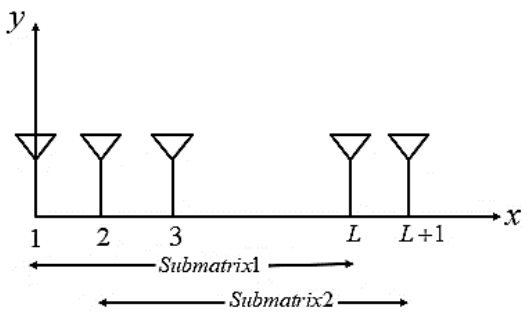

Figure 3.3 1D spatial smoothing method

$$Y_P = \begin{bmatrix} x(1) & x(2) & \ldots & x(N\text{-}L\text{+}1) \\ x(2) & x(3) & \ldots & x(N\text{-}L\text{+}2) \\ . & . & . & \\ . & . & . & \\ x(L) & x(L+1) & \ldots & x(N) \end{bmatrix} \tag{3.7}$$

Where, L represents the size of spatial smoothing window. This matrix is obtained by moving $N-L+1$ windows over the original signal X. In general, the length of L is from $N/2$ to $2N/3$. By the spatial smoothing method, the autocorrelation matrix of the signal is obtained:

$$R_P = E(Y \cdot Y^H) = \frac{1}{N_{obs}} Y_P \cdot Y_P{}^H \tag{3.8}$$

The eigenvectors of the autocorrelation matrix are divided into signal subspace corresponding to large eigenvalues and noise subspace corresponding to small eigenvalues. The $L \times (N-L+1)$ order autocorrelation matrix is expressed as:

$$R_P = S_P + W_p = AR_s A^H + \sigma^2 I = E_s \wedge_s E_s{}^H + \sigma^2 E_n E_n{}^H \tag{3.9}$$

The rank of the signal subspace [40] will have N non-zero eigenvalues. The last $L-1$ row of matrix Y is set as Y_1, and the first $L-1$ row of matrix Y is set as Y_2. Then there is a phase difference between two submatrices. As shown in Figure 3.4, Y_1 and Y_2 have the following relationship:

$$Y_2 = \phi Y_1 \tag{3.10}$$

where,

$$\phi = diag[\exp(j2\Pi\Delta f t_1)\ \exp(j2\Pi\Delta f t_2)\ \ldots\ \exp(j2\Pi\Delta f t_N)]$$

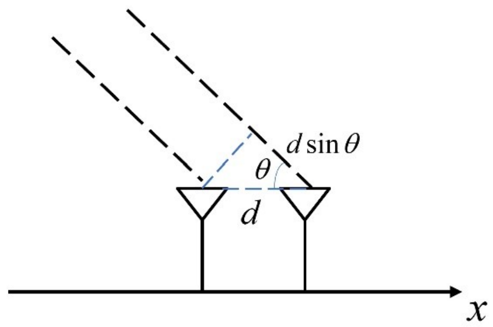

Figure 3.4 Subarray phase difference

This formula reflects the rotation invariance between the array flow patterns of two subarrays. Because $span\{E_s\} = span\{Y\}$, there is only a unique non-singular matrix T. We can get:

$$\begin{cases} E_{s1} = Y_1 T \\ E_{s2} = Y_2 T \end{cases} \tag{3.11}$$

Therefore, $E_{s2} = E_{s1}\psi$ is obtained, and we deduce that $\psi = E_{s1}{}^{+}E_{s2}$ [41]. The diagonal element of ψ is set as ζ, thus the location of 1D scattering center is deduced according to the following formula:

$$\exp(j\frac{4\Pi}{c}\Delta f^{(x)}x_n) = \zeta_n \tag{3.12}$$

When extending to 3D situation, it needs to consider smoothing direction sequence and scattering centers coordinates pairing. And the rest is consistent with the 1D method. According to the research in literature [42], there are three the scanning sequence methods $ord_1 = \{1,2,3\}, ord_2 = \{2,3,1\}, ord_3 = \{3,1,2\}$. As shown in Figure 3.5.

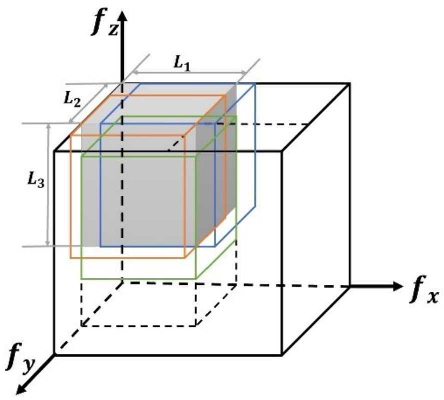

Figure 3.5 3D space smoothing method

The following is the Hankel matrix for spatial smoothing along the X-axis [43-44], and it is the same methods in other directions.

$$Y_x = \begin{bmatrix} Y_1^x & Y_2^x & \cdots & Y_{N-L+1}^x \\ Y_2^x & Y_3^x & \cdots & Y_{N-L+2}^x \\ . & . & . & \\ . & . & & . \\ Y_L^x & Y_{L+1}^x & \cdots & Y_N^x \end{bmatrix} \tag{3.13}$$

where,

$$Y_{\mathrm{m}}^x = \begin{bmatrix} \mathrm{y}_x(\mathrm{m,1}) & \mathrm{y}_x(\mathrm{m,2}) & \cdots & \mathrm{y}_x(\mathrm{m,T\text{-}P\text{+}1}) \\ \mathrm{y}_x(\mathrm{m,2}) & \mathrm{y}_x(\mathrm{m,3}) & \cdots & \mathrm{y}_x(\mathrm{m,T\text{-}P\text{+}2}) \\ . & . & . & \\ . & . & . & \\ \mathrm{y}_x(\mathrm{m,P}) & \mathrm{y}_x(\mathrm{m,P\text{+}1}) & \cdots & \mathrm{y}_x(\mathrm{m,T}) \end{bmatrix}$$

$$y_x(m,k) = \begin{bmatrix} \mathrm{D(m,1,k)} & \mathrm{D(m,2,k)} & \cdots & \mathrm{D(m,R\text{-}Q\text{+}1,k)} \\ \mathrm{D(m,2,k)} & \mathrm{D(m,3,k)} & \cdots & \mathrm{D(m,R\text{-}Q\text{+}2,k)} \\ . & . & . & \\ . & . & & . \\ \mathrm{D(m,Q,k)} & \mathrm{D(m,Q,k)} & \cdots & \mathrm{D(m,R,k)} \end{bmatrix}$$

Therefore, three scanning matrices are obtained by scanning the rearranged signals in different order. The coordinates information of hyperspace scattering center in each dimension are obtained successfully. The calculation formula of scanning matrix is as follows:

$$F_{ordk} = (\underline{V_s^{ordk}})^+ (\overline{V_s^{ordk}}) \quad k = 1,2,3 \tag{3.14}$$

Because we need to match the 3D coordinates, the diagonalization matrix F is derived through the linear combination of the three matrices. The unique non-singular matrix T is obtained through the diagonalization transformation:

$$F = a_1 F^{(ord_1)} + a_2 F^{(ord_2)} + a_3 F^{(ord_3)} = T^{-1} D T \tag{3.15}$$

where,

$$a_1 + a_2 + a_3 = 1$$

Therefore, we can get $\psi^{ord_k} = TF^{ord_k}T^{-1}$. The diagonal element of ψ^{ord_k} is also set as $\{\zeta_n^{ord_k}\}_{n=1..N}$. Locations are estimated by:

$$\begin{aligned} \exp(j\frac{4\Pi}{c}\Delta f^{(x)}x_n) &= \zeta_n^{ord_1} \\ \exp(j\frac{4\Pi}{c}\Delta f^{(y)}y_n) &= \zeta_n^{ord_2} \\ \exp(j\frac{4\Pi}{c}\Delta f^{(z)}z_n) &= \zeta_n^{ord_3} \end{aligned} \tag{3.16}$$

Locations can't distinguish the scattering center well in complex model. It needs to add amplitude information to assist judgment. The least square method is used to estimate the amplitude of scattering centers. The calculation formula is [45]:

$$A = (G^H G)^{-1} G^H E \tag{3.17}$$

where,

$$G(r_i) = \begin{bmatrix} \exp(-4\Pi jf(k_1)r_i / c) \\ \exp(-4\Pi jf(k_2)r_i / c) \\ \cdots \\ \exp(-4\Pi jf(k_b)r_i / c) \end{bmatrix}$$
$$i = 1, 2, ..., m$$

3.2.3 Sources number estimation

When the number of estimated sources is equal to the number of scattering centers, the performance of the algorithm is in the best state. The information theory methods that the Akaike Information Criterion (AIC) [46-48] and the Minimum Description Length (MDL) [49-50] are the classical algorithms in source estimation. The principle is that signal source numbers are calculated by examining the similarity of small eigenvalues. The information theory method based on AIC and MDL criteria [51] combines the logarithmic likelihood function composed of arithmetic and geometric mean of eigenvalues and different penalty functions and gives an estimate of the number of sources by minimizing this combination.

The specific operation is as follows. We suppose that signal $X(n)$ consists of m complex sinusoids plus white noise and its length is M . The maximum delay of its autocorrelation function is set as $P-1$. The autocorrelation matrix of its $p \times p$

dimension has P characteristic values and it arranges in order $\lambda_1 > \lambda_2 > ... > \lambda_p$.

The equation of the AIC is expressed as:

$$AIC(m) = 2N(P-m)\ln[\frac{g(m)}{a(m)}] + m(2P-m) \tag{3.18}$$

The equation of the MDL is expressed as:

$$MDL(m) = N(P-m)\ln[\frac{g(m)}{a(m)}] + \frac{1}{2}m(2P-m)\ln N \tag{3.19}$$

where,

$$g(m) = \prod_{i=m+1}^{p} \lambda_i^{\frac{1}{p-i}}$$

$$a(m) = \frac{1}{p-m}\sum_{i=m+1}^{p} \lambda_i$$

In formula 3.18 and formula 3.19, when i increases from 0 to $P-1$, m corresponding to minimum AIC(m) and minimum MDL(m) is the optimal number of signal source. The first term of the formula is obtained directly from the logarithmic likelihood function, and the second term is the penalty factor.

However, direct use of AIC and MDL criteria to estimate the number of sources is prone to overestimation, and the performance of conductance estimation is degraded. According to literature [52], SSAIC and SSMDL methods based on spatial smoothing method are obtained. They improve the probability of correct estimation. Formulas are as follows:

$$\begin{aligned} SSAIC(k) &= N(M_L-k)\ln(\frac{1}{M_L-k} * (\sum_{i=k+1}^{M_L} \overline{\lambda_i} / \left(\sum_{i=k+1}^{M_L} \overline{\lambda_i}\right)^{\frac{1}{M_L-k}})) + k(2M_L-k) \\ SSMDL(k) &= N(M_L-k)\ln(\frac{1}{M_L-k} * \sum_{i=k+1}^{M_L} \overline{\lambda_i} / \left(\sum_{i=k+1}^{M_L} \overline{\lambda_i}\right)^{\frac{1}{M_L-k}}) + \frac{1}{2}k(2M_L-k)\ln N \end{aligned} \tag{3.20}$$

Where, k represents scattering center estimation, M_L represents the number of eigenvalues, λ represents the eigenvalue and N represents sample number of quick beats.

3.2.4 Results

In this section, we use extensive models to analysis algorithm and all of them are simulated by full-wave algorithm. 1D simulation of three spheres has been considered. The positions are 0m, 5m and 13m respectively. The azimuth is 60°. The frequency range is from 9.7 GHz to 10.3 GHz, with 128 points.

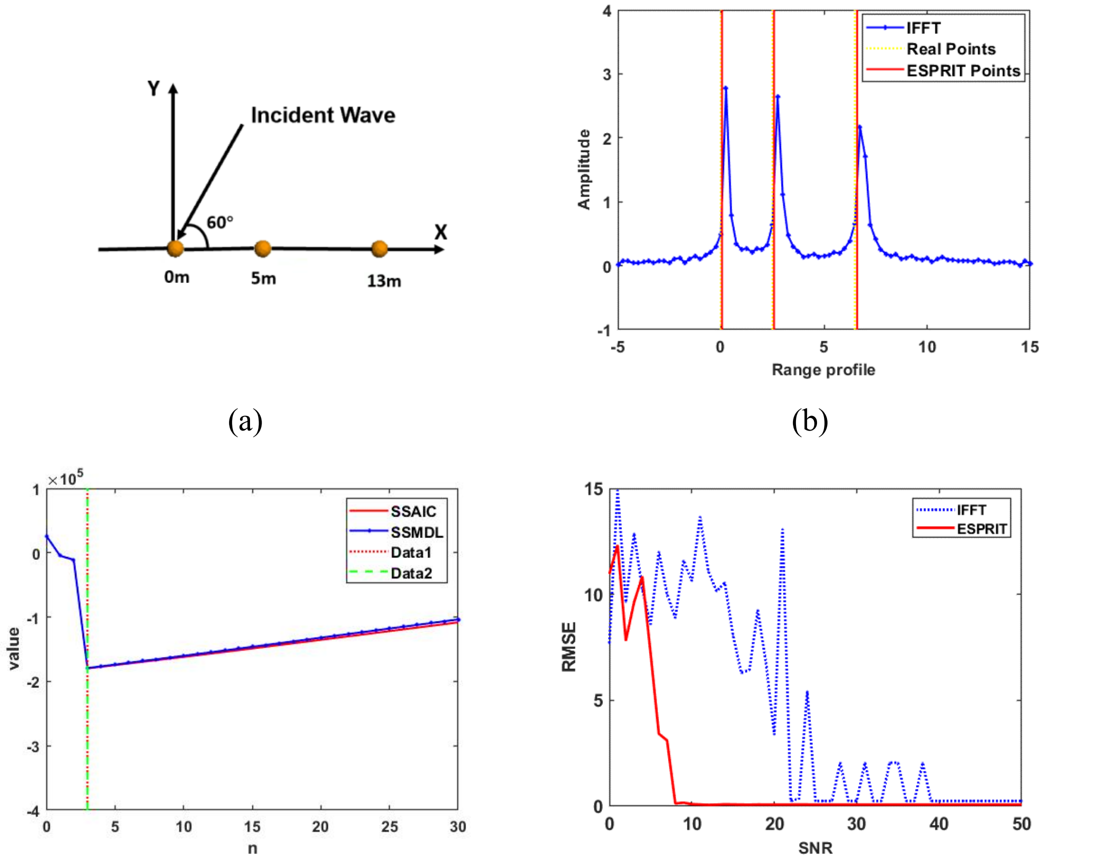

(a) (b)

(c) (d)

Figure 3.6 One dimension on three spheres. (a) Spheres model, (b) When SNR=30, the location of scattering points, (c) Judged source number, (d) RMSE under different SNR

Figure 3.6(b) shows the scattering centers locations extracted by IFFT and ESPRIT methods, but ESPRIT algorithm is relatively more accurate. In Figure 3.6(c), the x coordinate that corresponds to the minimum of the function is the optimal scattering number and $x=3$. Both SSAIC and SSMDL get accurate estimation. As shown in Figure 3.6(d), during the change of SNR from 0 to 50, RMSE of ESPRIT tends to 0 faster. ESPRIT has robustness to noise.

For 2D case, aircraft with 10m*10m*1m is simulated. Parameters are: Frequency range is from 9.7 GHz to 10.3 GHz; azimuth angles are from -1.5° to 1.5°; sampling points are 128*128.

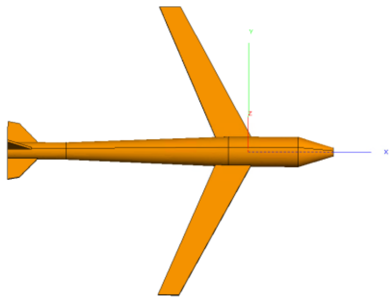

(a)

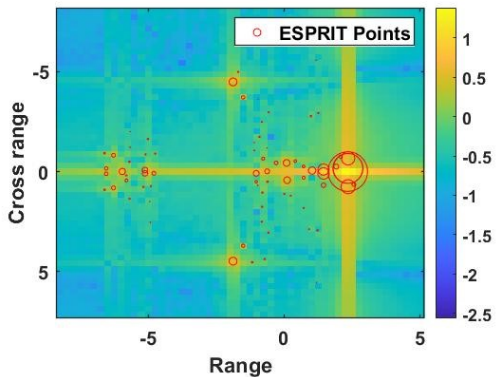

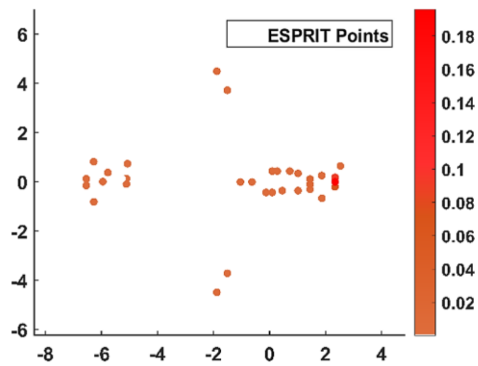

(b) (c)

Figure 3.7 Estimation of aircraft model, (a) Aircraft model, (b) Compared scatters extracted by ESPRIT with image by Fourier Transform, (c) 2D locations extracted by ESPRIT with amplitude

In Figure 3.7(b), the size of circle means amplitude. ESPRIT method performs well on extracting scattering centers of aircraft in Figure 3.7(c). Fourier radar image exists side-lobes, and ESPRIT method gets more detailed features.

For a scale reduced model of the aircraft is simulated in 3D case. Parameters are: Frequency range is from 9.5 GHz to 10.5 GHz; azimuth angles are from -2.87° to 2.87°; elevations are from 82.13° to 87.87°; Sampling points are 30*30*30. Wherein, the Radon transform is used to transform 3D image to the X-Y plane, X-Z plane and Y-Z plane.

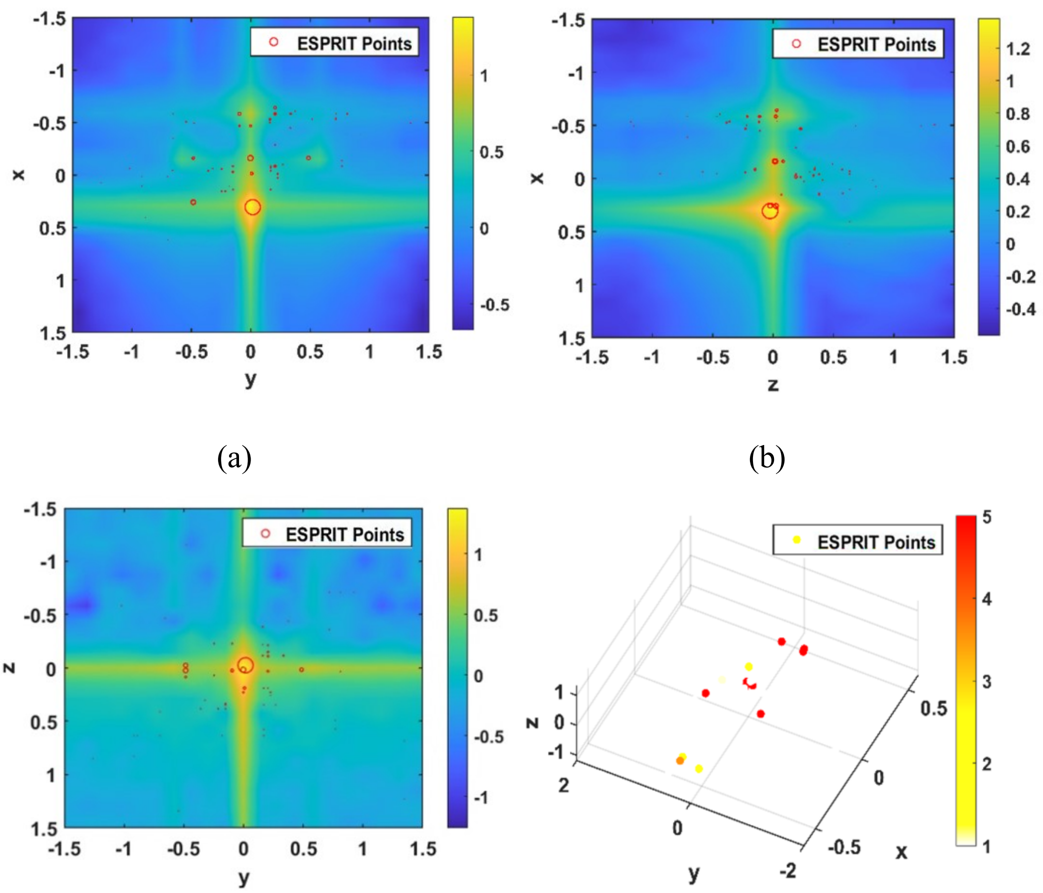

(a) (b)

(c) (d)

Figure 3.8 Scattering center estimation of 3D aircraft model, a) X-Y plane projection, b) X-Z plane projection, c) Z-Y plane projection, d)3D locations extracted by ESPRIT with amplitude

Figure 3.8 shows the resolution of 3D Fourier image is reduced due to the bandwidth and it can't well indicate the model features. 3D-ESPRIT method is not affected by the resolution, and the scattering field information is clearly expressed after the amplitude information added.

Thent we compare the CLEAN method and ESPRIT method. Complex aircraft model shows in Figure 3.9 is used to verify the algorithm. The aircraft model is 7m*6m*1m. Table 3.1 shows the parameters setting in FEKO software. And table 3.2 shows different results under different resolutions of two methods. When bandwidth is 2 GHz, the resolution is 0.075m. When bandwidth is 1 GHz, the resolution is 0.15m. We use traditional linear FFT method to generate image. Several experiments have shown that when the threshold is set as 70% energy of FFT image, the CLEAN algorithm works best for this aircraft model. ESPRIT method is used to extract scattering centers and reconstruct image. Results are shown in Table 3.2:

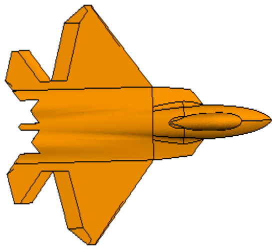

Figure 3.9 Aircraft model

Table 3.1 Parameters.

Target Parameter		Values	
Frequency Center f_0		10 GHz	
Elevation Angle		80°	
Frequency Samples		128	
Angular Samples		128	
B	9 GHz ~11 GHz	Azimuth Angle	-5.77° ~5.77°
B	9.5 GHz ~10.5 GHz	Azimuth Angle	-2.87° ~2.87°

Table 3.2 Results under different resolutions

Method/B	B=2 GHz	B=1 GHz
FFT Image	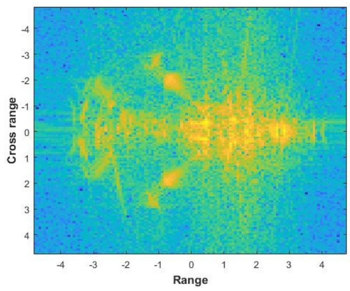	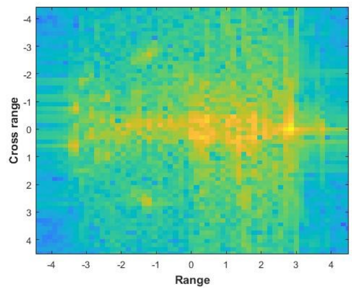
CLEAN	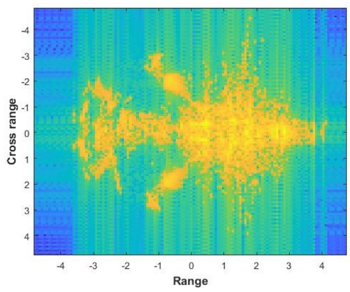	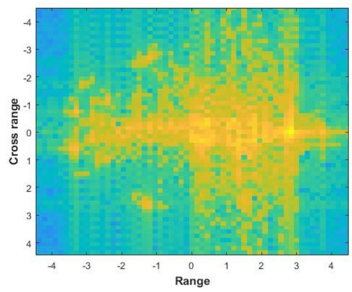

ESPRIT	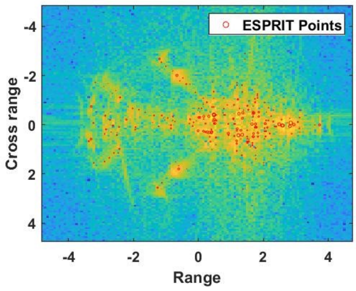	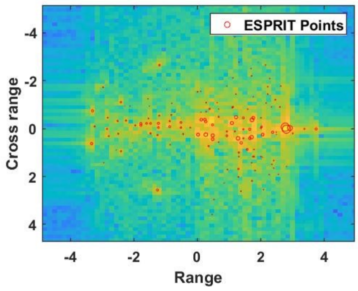

We can see when the resolution is small enough, both CLEAN algorithm and ESPRIT algorithm extract aircraft features well. But when the bandwidth is reduced by half, there are many sidelobes around the aircraft target extracted by CLEAN algorithm. And it cannot clearly display the aircraft characteristics. However, ESPRIT still accurately extract target centers at the same resolution. Therefore, compared with the CLEAN algorithm, ESPRIT algorithm is more flexible and suitable for various environments of radar targets.

3. 3 Conclusion

In this chapter, the ESPRIT algorithm is extended from one dimension to three dimensions and the simulation results of each dimension are given. The algorithm is verified from simple model to complex model, and locations of scattering center are accurately extracted. The amplitude of scattering center is calculated by the least square method. Comparison results of CLEAN and ESPRIT are also given. It proves ESPRIT has the advantages of not being limited by parameters and high stability.

Simulation results show that the ESPRIT method extracts specific physical information for each scattering center. In addition, the electromagnetic characteristics of various aspects are easily obtained by changing the parameters. Therefore, scattering center model is an effectively method to provide target database. And it is helpful to solve the problem of radar database scarcity.

Chapter 4 Scattering Image Recognition and Matching

Accurate classification of SAR images is beneficial to obtain military strategic advantage. The significance of electromagnetic simulation imaging is to provide a flexible and reliable target feature library for recognition system. This chapter uses domain matching method and neural network method to identify the simulation datasets.

To some extent, the spatial distribution of scattering centers represents the attitude of the image. The corresponding relationship between scattering centers and the image is shown by the domain matching method. Maximum likelihood method and newton iteration method [53] are used to estimate the scattering center parameters of the image to be recognized. Images are reconstructed according to the matching situation. And the similarity criterion is introduced as the discriminant criterion to estimate the similarity between SAR image and reconstructed image. This method is more simple and more effective than one-to-one matching of scattering centers.

In recent years, neural networks have made great achievements in image recognition. The improved Alex network is used to comprehensively learn the features of image generated by ESPRIT. The result shows that the classification rate of the simulation aircraft reaches 99.22%. Adding measured data into database, the rate reaches 99.39%. Then the corresponding visual interface is constructed to display the classification results intuitively.

4. 1 Domain matching method based on AML

4.1.1 AML algorithm

Approximate Maximum Likelihood (AML) is a statistical method for estimating parameters based on maximum likelihood principle. It was first proposed by the German mathematician Gauss in 1821. The detailed algorithms are given. For the unary real-valued variable x, the gaussian distribution is defined as:

$$N(x \mid \mu, \sigma^2) = \frac{1}{(2\pi\sigma^2)^{\frac{1}{2}}} \exp\{-\frac{1}{2\sigma^2}(x-\mu)^2\} \tag{4.1}$$

Where, $x = (x_1, x_2, ..., x_N)^T$ shows N observations of variable x, and each observation is assumed to be extracted independently from the gaussian distribution. The mean μ and the variance σ^2 of the distribution are unknown.

So the joint probability of the data is:

$$P(x \mid \mu, \sigma^2) = \prod_{i=1}^{N} N(x_i \mid \mu, \sigma^2) \tag{4.2}$$

Here we use maximum likelihood estimation to calculate the parameters of the gaussian distribution. The logarithmic likelihood function is:

$$\begin{aligned} \ln L &= \ln P(x \mid \mu, \sigma^2) \\ &= \ln \prod_{i=1}^{N} N(x_i \mid \mu, \sigma^2) \end{aligned} \tag{4.3}$$

Substituting the distribution function, and the logarithmic likelihood function becomes:

$$\begin{aligned} \ln L &= \ln P(x \mid \mu, \sigma^2) \\ &= -\frac{1}{2\sigma^2}\sum_{n=1}^{N}(x_n-\mu)^2 - \frac{N}{2}\ln\sigma^2 - \frac{N}{2}\ln(2\pi) \end{aligned} \tag{4.4}$$

The partial derivatives of the likelihood function are shown in follows:

$$\begin{aligned} \frac{\partial \ln L}{\partial \mu} &= \frac{1}{\sigma^2}\sum_{i=1}^{N}(x_i-\mu) = 0 \\ \frac{\partial \ln L}{\partial(\sigma^2)} &= -\frac{N}{2\sigma^2} + \frac{1}{2\sigma^4}\sum_{i=1}^{N}(x_i-\mu)^2 = 0 \end{aligned} \tag{4.5}$$

The solution of μ is obtained from the first equation:

$$\mu_{MLE} = \frac{1}{N}\sum_{i=1}^{N} x_i \tag{4.6}$$

Formula 4.6 is substituted into the second equation, and the solution to σ^2 is:

$$\sigma_{MLE}{}^2 = \frac{1}{N}\sum_{i=1}^{N}(x_i-\mu_{MLE})^2 \tag{4.7}$$

In general, parameter estimation of the maximum likelihood method generally includes the following steps:

(1) Finding the likelihood function. Calculating the log-likelihood function of the distribution according to the probability density function.

(2) Finding $\ln L(\theta)$ and likelihood equation. The logarithmic likelihood function takes the derivative of the parameter and the derivative tends to zero:

$$\frac{\partial \ln L(\theta)}{\partial \theta_i} = 0 \quad \text{(i=1,2,...,m)} \tag{4.8}$$

(3) Getting the maximum likelihood estimation. Solving the equations and getting the estimated value of the parameters:

$$\hat{\theta}_i = \hat{\theta}_i(x_1, x_2, ..., x_n) \quad \text{(i=1,2,...,m)} \tag{4.9}$$

4.1.2 Two-dimensional image to be identified

This section describes the electromagnetic models and the scattering center characteristics of three similar aircrafts, F35, F22 and F16. F35 aircraft is 15.47m (length) ×10.7m (width) ×4.57m (height), F22 aircraft is 18.9m×13.56m×5.08m and F12 aircraft is 16.47m×9.75m×5.43m. In the simulation imaging, three models are scaled in the same proportion.

In the 2D case, the scattering center model is used to parameterize the electromagnetic scattering model. Model as follows [54]:

$$\begin{aligned} E^{Model}(f, \beta; \Theta) &= \sum_{k=1}^{N} E_k(f, \beta; \theta_i) \\ &= \sum_{k=1}^{N} A_k \exp(j \frac{4\Pi}{c} f(x_k \cos\beta + y_k \sin\beta)) \end{aligned} \tag{4.10}$$

where,

$$\Theta = \{\theta_k\} = \{A_k, x_k, y_k\} \quad \text{i=1...N}$$

We can obtain a large number of simulation images through models in different poses, it is very flexible. When the pitching angle is 85° and the azimuth angle is 0°, Figure 4.1 shows the 2D simulation image and ESPRIT image of various aircraft. The location of the scattering center is a good reflection of the geometry information of each target. Similarly, the relation between the simulation image and ESPRIT image of F35 model at different rotation angles is given. When the attitude of the target changes, the spatial distribution of the scattering center also changes. The results show that ESPRIT image has strong correlation with electromagnetic simulation image. And it also shows the effectiveness of the established 2D electromagnetic scattering model [55].

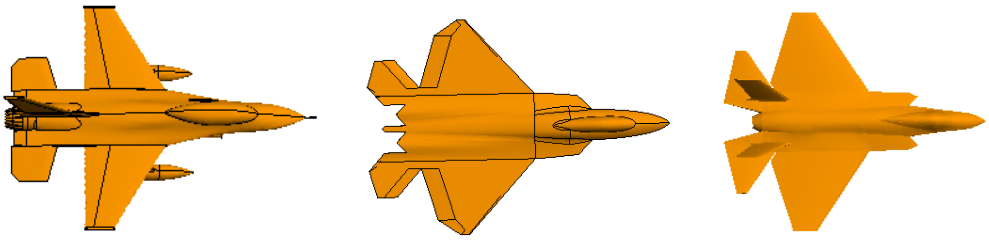

(a) (b) (c)

Figure 4.1 CAD model. (a)F16 model, (b) F22 model, (c) F35 model

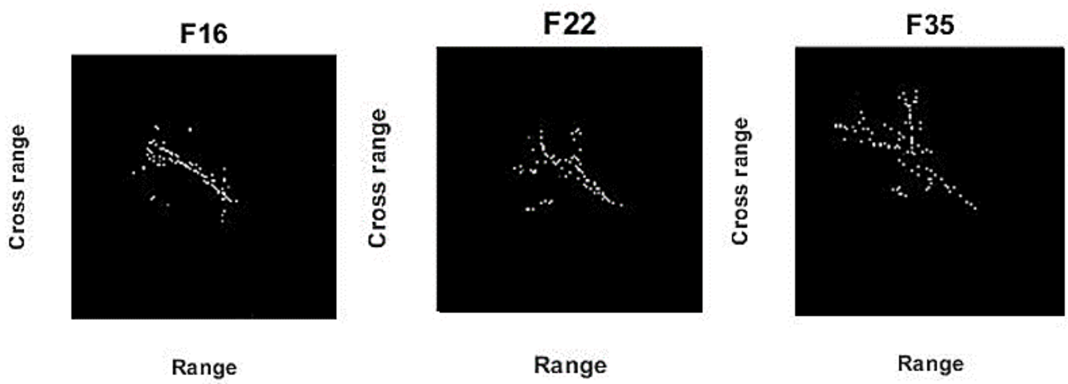

(a) (b) (c)

Figure 4.2 ESPRIT image. (a)F16 model, (b) F22 model, (c) F35 model

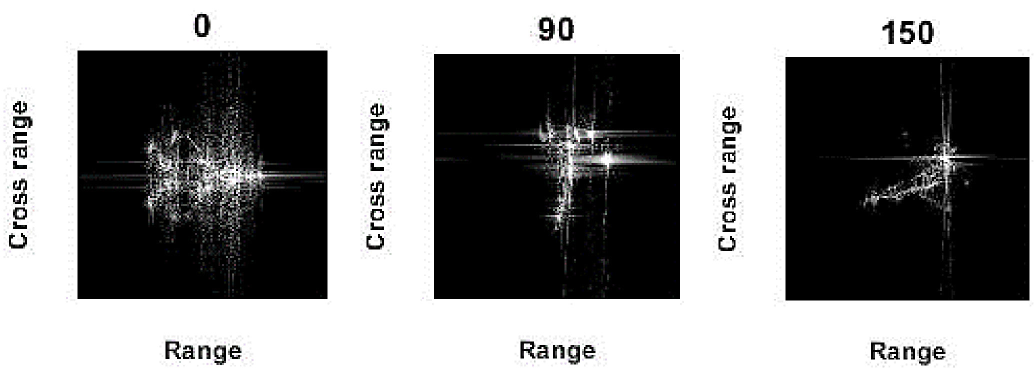

(a) (b) (c)

Figure 4.3 FFT Images of F35 at different azimuth angle. (a)0° , (b)90° , (c)150°

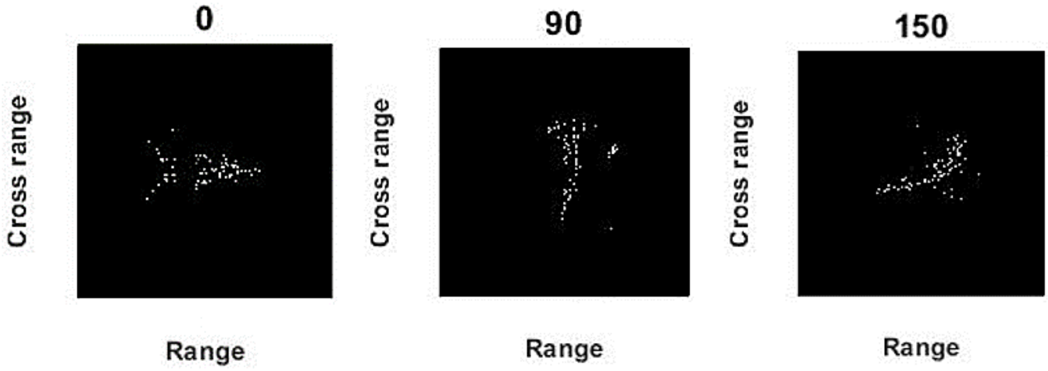

(a) (b) (c)

Figure 4.4 ESPRIT images of F35 at different azimuth angles. (a)0°, (b)90°, (c)150°

4.1.3 Recognition based on domain matching

Similar to formula 3.2, the measured signal received is equivalent to the sum of target signal and noise signal (such as sensor noise). And the noise is gaussian white noise. The measurement signal expression is as follows [56]:

$$D(f,\phi) = E(f,\phi;\Theta) + N(f,\phi) \tag{4.11}$$

Fourier transform is used to transform the measurement signal into the image domain:

$$\begin{aligned} &FFT(D(f,\phi)) = FFT(E(f,\phi;\Theta) + N(f,\phi)) \\ &D(x,y) = E(x,y;\Theta) + N(x,y) \end{aligned} \tag{4.12}$$

Since the Fourier transform is a linear operation, $N(x,y)$ also satisfies the properties of gaussian white noise. Therefore, the values of parameter Θ are estimated by $D(x,y) - E(x,y;\Theta)$.

AML method provides a model parameter estimation method based on observed data. We use this method to estimate scattering center parameters, such as position and amplitude [57-60]. For real SAR data $B(f,\phi)$, the parameter estimation problem of the attributed scattering center contained in SAR data is expressed as:

$$\begin{aligned} &\Theta_{AML} = \arg\min J(\Theta) \\ &J(\Theta) = [D - E(\Theta)]^H \sum{}^{\dagger} [D - E(\Theta)] \end{aligned} \tag{4.13}$$

Where, D, $E(\Theta)$ and N are vectors obtained by stacking the columns of

$D(x, y)$, $N(x, y)$ and $E(x, y;\Theta)$ [56]. $\sum \mathrm{cov}(N)$ and $()^{\dagger}$ mean Moore-Penrose pseudo inverse. Because the simulation image generated by the target is composed of multiple scattering centers, the scale of attribute parameters to be estimated is large and the calculation is complicated. We consider dividing the image into multiple small regions. It divides the big problem into small problems and reduces the calculation.

Watershed algorithm [61] is a classical image region segmentation method. And it uses mathematical morphology and topology theory. The principle is to connect the pixels with similar positions and similar gray values to form a closed region by calculating the gray similarity between adjacent pixels. Thus, this method is used to decompose the image to be recognized into several small regions R . Each small region contains a very small number of scattering centers. Curve fitting is carried out for each region, and the local minimum value is taken at the convergence point of the function to achieve maximum likelihood solution for a single scattering center.

$$\begin{aligned} &\Theta_{AML} = \arg\min J(\Theta) \\ &J(\Theta) = [R - E(\Theta)]^{H} \sum{}^{\dagger} [R - E(\Theta)] \end{aligned} \tag{4.14}$$

The domain matching method is used to initially correlate the attribute scattering centers of the recognized samples with ESPRIT images. The scattering center extracted from the image is the center of the circle, and setting an effective radius R . When the scattering center in ESPRIT image is located inside the circle, the match is judged to be successful. Then the successfully matched points are extracted to reconstruct the image and it is beneficial to standardize the datasets. The flow chart of domain matching is shown in Figure 4.5:

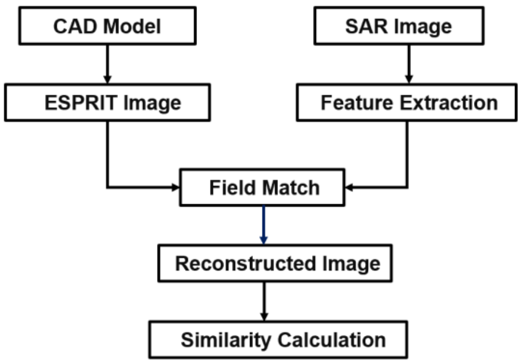

Figure 4.5 Flow chart of domain matching

The simulation image of F35 is set as the image to be recognized, and the similarity is compared with ESPRIT image of F35, F22 and F16 respectively. Figure 4.6 shows the matching results under different radii.

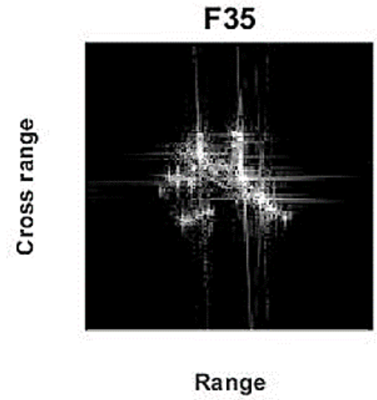

(a)

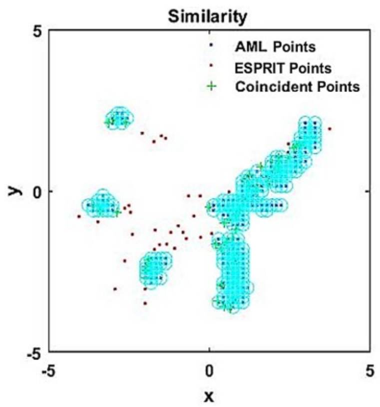

(b)

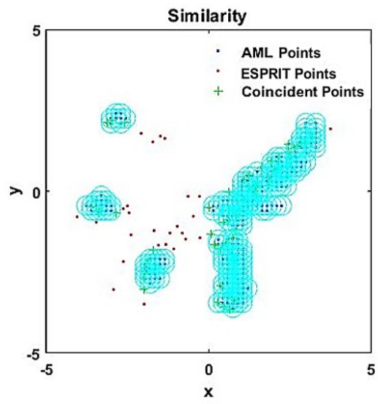

(c)

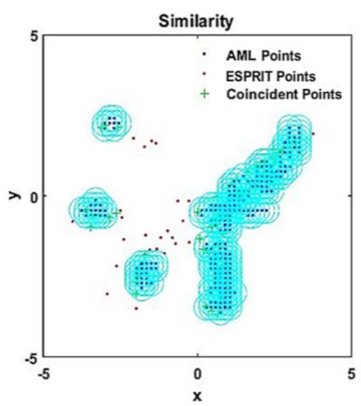

(d)

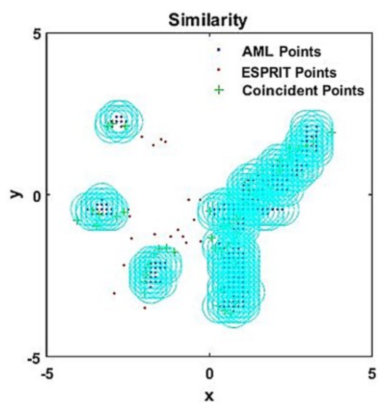

(e)

Figure 4.6 The coincidence of F35 simulation image and F35 ESPRIT image under different radii. (a)2D simulation image of F35, (b) R=0.2, (c) R=0.3, (d) R=0.4, (e) R=0.5

The overlapping scattering centers are extracted and the images are reconstructed.

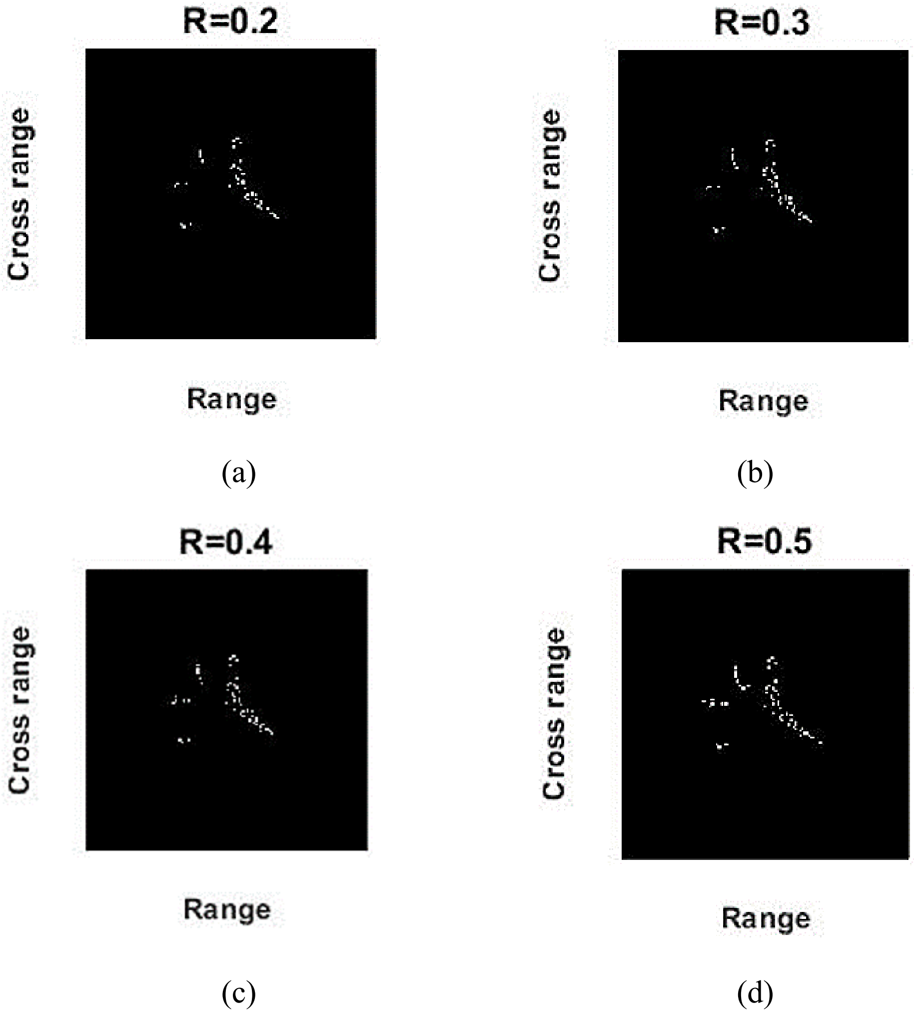

Figure 4.7 Reconstructed image of F35. (a) R=0.2, (b) R=0.3, (c) R=0.4, (d) R=0.5

The figure below shows when $R = 0.3m$, the radius matching results of F35 image with other ESPRIT images:

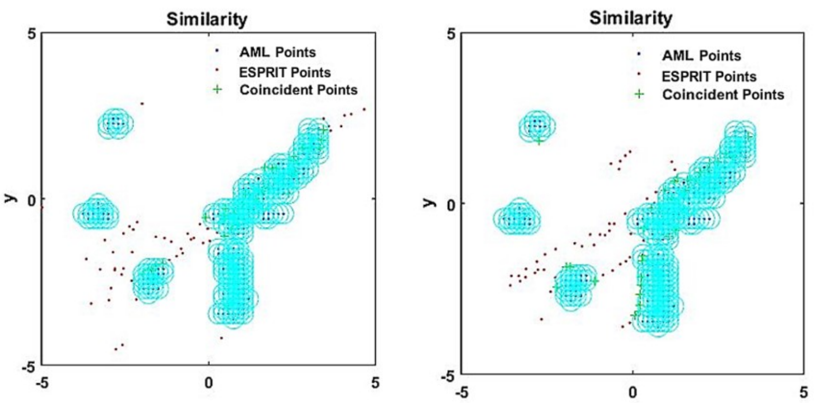

(a) (b)

Figure 4.8 The coincidence of F35 simulation image and the ESPRIT images of other aircrafts under different radius. (a) F22, (b)F16

Similarly, using the overlapping scattering centers to reconstruct image:

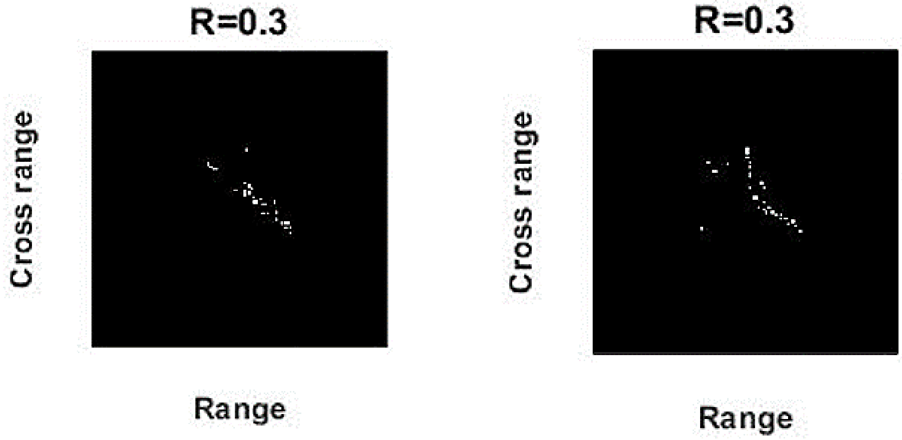

(a) (b)

Figure 4.9 The reconstructed images of different aircrafts. (a) F22, (b)F16

The matching scattering centers of the model reflect the correlation and differences between the image to be recognized and the ESPRIT image.

Under the same parameters, the similarity between reconstructed image and electromagnetic image is calculated to achieve the objects classification. The basic similarity is the degree of image correlation between the image to be recognized and the image reconstructed by the model, and a certain weight is added to the basic similarity. Thus, the similarity criterion is constructed to estimate the correlation between the image to be recognized and the reconstructed image. The similarity formula is defined as [55]:

$$\begin{aligned} g(I_r, I_R) &= Cor(I_r, I_R) * \frac{M_1}{M_2} \\ &= \frac{\sum_x \sum_y [I_r(x,y) - g_1][I_R(x-\Delta x, y-\Delta y) - g_2]}{[\sum_x \sum_y [I_r(x,y) - g_1]^2 [I_R(x-\Delta x, y-\Delta y) - g_2]^2]^{1/2}} * \frac{M_1}{M_2} \end{aligned} \tag{4.15}$$

Where, M_1 is the number of reconstructed images and M_2 is the number of centers extracted from the image. $Cor(I_r, I_R)$ [62] calculates the image correlation between the two images. g_1 and g_2 are the gray mean values of I_r and I_R respectively. Similarity evaluation result is shown in Figure 4.10.

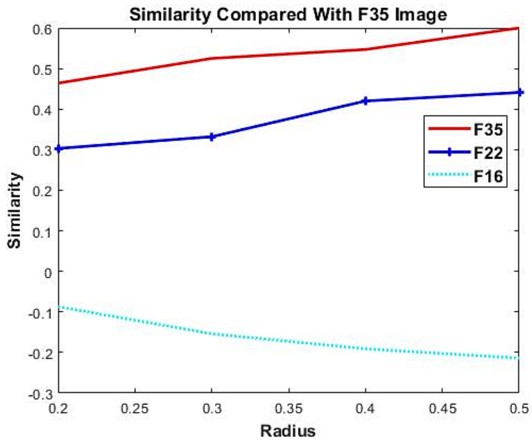

Figure 4.10 Similarity comparison

In above figure, the matching results of other ESPRIT images and F35 image have low similarity under the same radius. The scattering centers cannot be matched. Therefore, we conclude that the domain matching methods provide a basis for correctly distinguishing different types of targets. In addition, the matching value basically increases with the radius. But it is necessary to choose a reasonable radius. If the matching radius increases infinitely, scattering centers of any model will be in the effective radius neighborhood. It will increase difficulty to distinguish targets.

4.1.4 Conclusion

In this section, the field matching method is used to match the ESPRIT image and the electromagnetic image to be identified. The principle is to extract as much useful information as possible from the model to reconstruct the target. And it makes full use of the correlation between scattering center distribution and model to identify the target. Although the method is not precise enough, compared with the one-to-one matching method between scattering centers, the calculation is simple and the matching efficiency is greatly improved. And the validity of ESPRIT method in target recognition is also proved.

4. 2 Neural network recognition

Recently, deep learning has been widely concerned by the academic community in image classification field. It uses network structure to automatically extract rich feature information layer by layer and effectively solves the problem of difficult feature extraction before.

In this section, simulation data and measured data are processed by ESPRIT method. And we take the ESPRIT image as input of the improved ALEX network. The importance of ESPRIT method in network identification is highlighted.

4.2.1 Basic structure of neural network

Neural networks have the following basic structures:

(1) Input layer

The input of CNN network is the 2D image, and image features are gradually extracted from low-level to high-level.

(2) Convolution layer

The function of the convolution layer is to extract image features. Adopting different convolution kernel to convolved with objects, and it will extract different feature map with different features. In the process of convolution operation, parameters such as stride and convolution kernel size need to be set. One of the properties of the convolution kernel is locality. It only focuses on local features, and the degree of local depends on the size of the convolution kernel.

The convolution input layer of multiple 2D SAR images is assumed as $x \in R^{k \times w}$. h and w represent the height and width of the images respectively. The specific calculation formula is as follows:

$$y_{i^{'} j^{'}} = f(b + \sum_{i=1}^{h} \sum_{j=1}^{w} W_{ij} \times x_{i^{'}+i, j^{'}+j}) \tag{4.16}$$

Where, the input is x and parameter W is the weight in each layer, b represents the bias term, and $f(\bullet)$ is a nonlinear activation function. Sigmoid function is used and its value range is [0,1]. The formula is as follows:

$$f(x) = \frac{1}{1+e^{-x}} \tag{4.17}$$

(3) Pooling layer

When pooling is applied to the convolution layer, the output of feature vectors will be reduced. The result is improved and the over-fitting state is not easy to occur. Commonly filter size is 3*3, 2*2, and the stride are 2. Filter size should not be too large, otherwise it will lead to information loss. There are two common pooling modes, maximum pooling and average pooling. Maximum pooling selects the maximum value from all pixels [63]. The maximum pooling function is:

$$y_{i^{'}j^{'}} = \max_{1<i<k,1<j<w} x_{i^{'}+i,j^{'}+j} \tag{4.18}$$

Average pooling is taking the average of pixel values. The mean pooling function is:

$$y_{i^{'}j^{'}} = \underset{1<i<k,1<j<w}{avg} x_{i^{'}+i,j^{'}+j} \tag{4.19}$$

(4) Full connection layer

After the input image is convolved and pooled, the original data is mapped to a high-dimensional feature space, and more representative features are extracted. The obtained 2D feature pattern is drawn into a vector and it is fully connected with the output layer [63].

(5) Output layer

The main function of this layer is classification. The feature vector of the whole connection layer is classified and identified as the input of the output layer. The output value of this layer represents the probability of each category. There are some commonly classifiers. Such as Softmax classifier, SVM classifier, decision tree classifier, and random forest classifier.

4.2.2 The improved ALEX network

As shown in the Figure 4.11, the depth of Alex network is 8-layer structure. The first 5 layers are convolution layers and the last 3 layers are fully connected layers. There are 60 million learning parameters and 650,000 neurons [64]. It is an order of magnitude larger than any previous CNN training. Because ESPRIT image features are sparse, we use a small number of convolution layers to extract information. And the architecture of our model is shown in Table 4.1

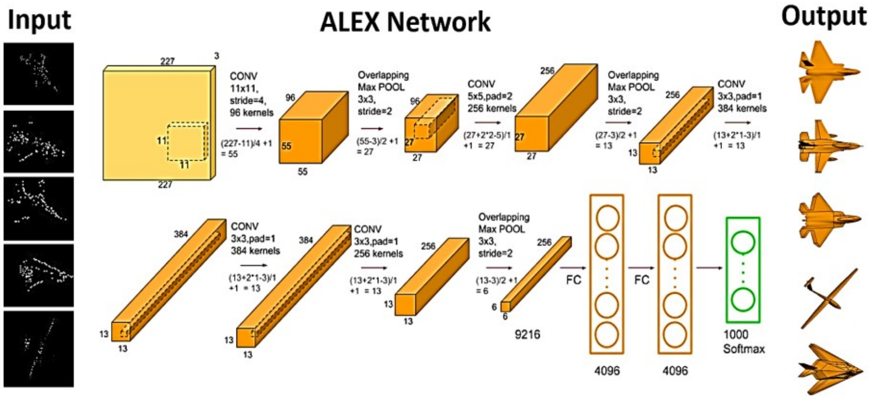

Figure 4.11 The structure of Alex network

Table 4.1 Each architecture of our model

Input	Input code	128*128*1
Firstly Layer	TranConv1	4*4
	Relu	True
	MaxPooling	3*3
	BatchNormalization	
Secondly Layer	TranConv2	4*4
	Relu	True
	BatchNormalization	
Thirdly Layer	Dropout	0.5
	Linear	
	Relu	True
Fourth Layer	Dropout	0.5
	Linear	
	Relu	True
Fifth Layer	Linear	

The steps are as follows. We build five aircraft models by FEKO software. And parameters are: Incident frequency range is from 9.5 GHz to 10.5 GHz; the pitch angle is 80 degrees; sampling numbers are 128*128. And an image is generated every 2 degrees of azimuth from 0 degree to 180 degrees. Then using data enhancement methods to expand the original data samples and create more data. We use rotation, stretching, cutting and other methods to expand the original data samples, so as to have a better performance in the training process.

We put data into the improved ALEX network for training [65]. The learning rate is set as 0.003 and dropout is 0.5. The software system adopts the Pytorch experimental framework. Based on GPU1080TI hardware environment. There are 1915 images in the datasets, of which 80 percent of the data samples (1532 images) are used for training, and 20 percent (383 images) for testing, with a consistent number for each category.

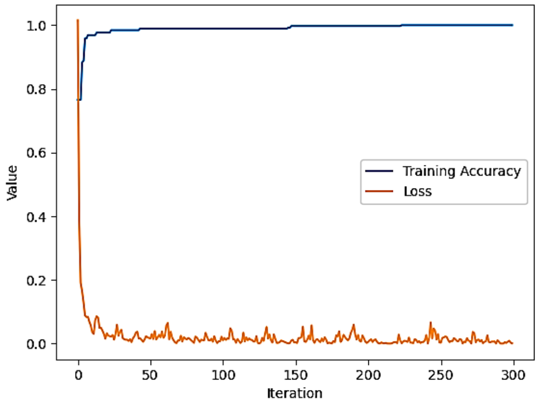

Figure 4.12 The result of Alex network

Table 4.2 The recognition result of each aircraft model

Classes/ Numbers						Accuracy
	75	0	0	0	2	97.40%
	0	76	0	1	0	98.70%
	0	0	76	0	0	100%
	0	0	0	77	0	100%
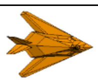	0	0	0	0	77	100%
Average Accuracy						99.22%

Accuracy and loss degree are used to evaluate the convergence of the model. In

Figure 4.12, training accuracy basically remains unchanged at the 240th period. Therefore, we deduce that the network achieves a stable state and the final accuracy is 99.22%. Table 4.2 shows the recognition rate of each aircraft model. This highlights that the database generated by ESPRIT is well classified in our network.

To test the effectiveness of recognition under real conditions, we obtain the measured data of aircraft model 3 in the microwave anechoic chamber. Parameters are: Incident frequency range is 9 GHz to 10 GHz; the pitch angle is 10 degrees; sampling numbers are 100*100. And an image is generated every 2 degrees of azimuth from 0 degree to 360 degrees. Using ESPTIR method to extract scattering centers and also using same data enhancement methods to process ESPRIT images, then we get 710 real images. And part of the measured images are shown below:

Table 4.3 Measured data processing results of aircraft 3

FFT Image	ESPRIT Image	Expanded Image
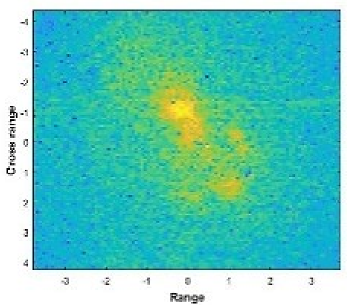		

From Table 4.3, we can see FFT image of measured data contains a lot of noise and features are not prominent. These unnecessary features will affect the training accuracy of the network. For comparison, the ESPRIT algorithm only extracts the important characteristics of the target, and each scattering center represents unique physical characteristics of the object, such as azimuth information. The effect of sidelobe on the network is greatly reduced. Then the measured data and the simulation data are put together as the network training set, and our network processing result is:

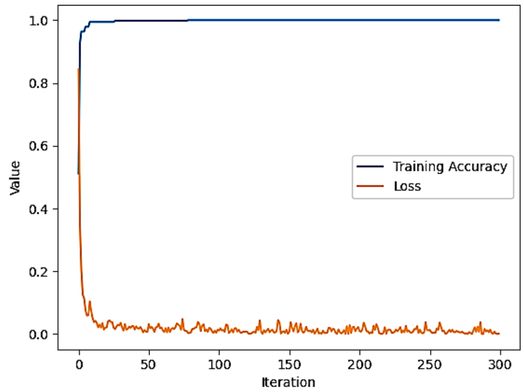

Figure 4.13 The result of mixed data in Alex network

Table 4.4 The recognition rate of mixed data

Classes/ Numbers						Accuracy
	76	0	0	1	0	98.70%
	0	76	0	1	0	98.70%
	0	0	76	0	0	100%
	0	1	0	218	0	99.54%
	0	0	0	0	77	100%
Average Accuracy						99.39%

Mixed data means adding measured data to the original datasets. The results show accuracy of the network is 99.39%. It means that ESPRIT reduces the impact of noise in the real environment and realizes high precision extraction of target scattering centers characteristics. And it also indicates that the datasets generated by ESPRIT have the potential to be effectively identified in the real environment.

4.2.3 Development of aircraft target classification system

After obtaining the classification results of five types of aircraft, a visual interface is built to show the classification result of neural network more intuitively. This section uses PyQt language to develop the system interface. The visual interface includes four main parts. Image import button, image display interface, classification button and result display. Importing image of any of the five targets, and this system accurately displays its category.

The visualization result is displayed as follows：

Figure 4.14 The classification system

4. 3 Conclusion

This chapter mainly introduces the classification methods. The field matching method based on AML is introduced first. According to the physical characteristics of the scattering center, the ESPRIT image is matched with the 2D image to be recognized in different radii. We use the similarity criterion to judge the correlation between the electromagnetic image and the reconstructed image. In addition, because neural network can extract scattering image features automatically, the datasets of five aircrafts generated by ESPRIT are classified by the improved Alex network. And corresponding spatial target classification visual interface is constructed to better display the classification results.

Chapter 5 Summary and Prospect

5. 1 Summary

Accurate reconstruction and target recognition are always the focus of radar research. This thesis first studies the reconstruction of high-resolution image. The high-resolution algorithm is compared with traditional imaging algorithm, and the corresponding database is provided for subsequent target recognition. Next the domain matching method and the improved ALEX network are used for electromagnetic image classification and recognition. Final the visual interface is constructed to clearly display the target classification results.

From theoretical derivation to simulation practice, the main contributions of this thesis are as follows:

The electromagnetic field data is calculated by PO method, and the 3D image is obtained by Fourier transform method. Because the FFT imaging requires the beam domain data to be uniform data, the original electromagnetic field data are interpolated to achieve the 3D imaging. The results show that FFT method is faster than the direct imaging method.

For the scattering center reconstruction, the CLEAN algorithm is introduced to extract the scattering center first. However, due to the limitation of resolution parameters, the reconstructed image is distorted to some extent. Thus, the super-resolution ESPRIT algorithm is proposed. And the comparison results with CLEAN algorithm and FFT algorithm are given. This method is of great significance to the extraction of scattering centers of complex targets and is suitable for most scattering mechanisms. It also provides a database for target identification.

For target recognition, every scattering center contains rich physical information. And it represents the change information of objects. Therefore, the similarity between the electromagnetic image to be recognized and ESPTIT image is obtained by using the domain matching method. Next, the database processed by ESPRIT method have high accuracy in the improved ALEX network. This shows that ESPRIT plays a positive role in target recognition. Final the classification visual boundary is created.

5. 2 Prospect

Electromagnetic imaging technology is a combination of electromagnetic simulation and radar imaging technology. Through the combination of electromagnetic calculation and signal processing, high precision image is obtained. Based on the research results of this thesis, the future work is carried out as follows:

Firstly, although the 3D ESPRIT algorithm realizes the 3D reconstruction of complex objects in space, it has a large amount of computation and slow speed. Therefore, a fast parameter estimation algorithm for scattering center model will be a key research direction in this field.

Secondly, the maximum likelihood method and newton iteration method are used to estimate scattering centers information, and the calculation are simple and fast. However, due to the influence of noise, the main part of the image can’t be accurately extracted. This has a negative impact on subsequent target matching. Therefore, the accurate estimation of scattering center parameters needs further research.

Lastly, there are still some problems such as poor classification results in the neural network recognition. Radar image recognition methods mostly come from optical image recognition methods. We can consider the combination of network and the physical characteristics of radar image, and it will improve the identification accuracy.

Reference

[1] Prickett M J, Chen C.C. Principles of inverse synthetic aperture radar /ISAR/ imaging[J]. IEEE Eascon Record, 1980.

[2] Nian Y H. Research on ISAR 3D imaging of nonuniform linear array[D]. Harbin Institute of Technology, 2018.

[3] Wang X. Super resolution ISAR imaging based on unitary ESPRIT and its application[D]. Xidian University, 2015.

[4] Schmidt R. Multiple emitter location and signal parameter estimation. IEEE Transactions on Antennas and Propagation, vol. 34, no. 3, pp. 276-280, March 1986.

[5] Delisle G Y, Wu H. Moving target imaging and trajectory computation using ISAR[J]. IEEE Transactions on Aerospace & Electronic Systems, 1994, 30(3): 887-889.

[6] Eerland K K. Application of Inverse synthetic aperture radar on aircraft[C]. New York: Proc. IEE-F. 1993, 140(1), P. 1-1.

[7] Bromaghim D R, Perry J P. A Wideband Linear FM Ramp Generator for the Long-Range Imaging Radar[J]. IEEE Transactions on Microwave Theory & Techniques, 1978, 26(5): 322-325.

[8] Ausherman D A, KOZMA A, et al. Developments in Radar Imaging[J]. IEEE Transactions on Aerospace and Electronic Systems, July 1984, 20(4): 363~400.

[9] Chen C, Andrews H. Target-motion-induced radar imaging[J]. IEEE Transactions on Aerospace and Electronic Systems, 1980, 16(1): 2-14.

[10] Chen C, Andrews H. Multifrequency imaging of radar turntable data[J]. IEEE Transactions on Aerospace and Electronic Systems, 1980, 16(1): 15-22.

[11] Li Y, Wu R, Xing M, et al. Inverse synthetic aperture radar imaging of ship target with complex motion[J]. Radar Sonar Navigation, 2008, 2(6): 395-403.

[12] Chen V C, Qian S. Joint time-frequency transform for radar Range-Doppler imaging. IEEE Transactions on Aerospace and Electronic Systems. 1998, 34(2): 486-499.

[13] Chen V C. Adaptive time-frequency ISAR processing. International Society for Optical Engineering (SPIE) 1996, 2845: 133-140.

[14] Roy R, Paulraj A and Kailath T. ESPRIT--A subspace rotation approach to estimation of parameters of cisoids in noise. IEEE Transactions on Acoustics Speech & Signal Processing, vol. 34, no. 5, pp. 1340-1342, October 1986.

[15] Zoltowski M D, Haardt M and Mathews C.P. Closed-form 2-D angle estimation with rectangular arrays in element space or beamspace via unitary ESPRIT. IEEE Transactions on Signal Processing, vol. 44, no. 2, pp. 316-328, Feb. 1996.
[16] Haardt M and Nossek J. A 3-D unitary ESPRIT for joint 2-D angle and carrier estimation[C]. 1997 IEEE International Conference on Acoustics, Speech, and Signal Processing, 1997, pp. 255-258 vol.1.
[17] Liu Q, Wang X S. Two-dimensional virtual ESPRIT algorithm[J]. Journal of National University of Defense Technology, 1999.
[18] Feng D J, Wang X S, Chen Z J, et al. Unitary ESPRIT super-resolution ISAR imaging Method[J]. Acta Electronica Sinica, 2005.
[19] Wang L, Li G L, et al. A new single-shot two-dimensional ESPRIT algorithm. Transactions of Beijing Institute of Technology, 2013(01):99-104.
[20] Liu S, Zhang G, Weng M and Yang S. Unified ESPRIT spatial spectrum for Direction-of-Arrival estimation with an arbitrary sparse array. 2016 IEEE 13th International Conference on Signal Processing, 2016, pp. 457-461.
[21] Zhang X K, Zheng S Y, Xi Z F, Ge Q C, Zong B F. Parameter Estimation and RCS Reconstruction of GTD Model based on improved LS-ESPRIT Algorithm[J]. Journal of electronics and information technology,2020,42(10):2493-2499.
[22] Pi Y M, Yang J Y, et al. Synthetic Aperture Radar Imaging Principle. University of Electronic Science and Technology of China Press, 2008,47-48.
[23] Yao R. Research on Inverse synthetic aperture Radar imaging[D]. Nanjing University, 2012.
[24] Stratton J A, Chu L J. Diffraction Theory of Electromagnetic Waves[J]. Physical Review, 1939, 56(1):99-107.
[25] Ufimtsev P Y. Elementary edge waves and the physical theory of diffraction[J]. Electromagnetics 11(2):125-159, April 1991.
[26] Gordon, W. Far-field approximations to the Kirchoff-Helmholtz representations of scattered fields[J]. IEEE Transactions on Antennas & Propagation, 1975, 23(4):590-592.
[27] Burkholder R J. Fast physical optics integration for rough surface scattering. Antennas & Propagation Society International Symposium IEEE, 2003.
[28] Weinmann F. Ray Tracing With PO/PTD for RCS Modeling of Large Complex Objects[J]. IEEE Transactions on Antennas & Propagation, 2006.
[29] Shi K. Research on super-resolution reconstruction algorithm of remote sensing

image[D]. Xi 'an University of Science and Technology,2020.
[30] Bao Z, Xing M D, Wang T, Radar imaging technology[M]. Beijing: Publishing of electronic Industry 2005.
[31] Deans S R. The Radon transform and some of its applications，John Wiley and Sons., 1983.
[32] Beylkin G. Discrete radon transform. IEEE Transactions on Acoustics Speech & Signal Processing, vol. 35, no. 2, pp. 162-172, 1987.
[33] Roy R and Kailath T. ESPRIT-estimation of signal parameters via rotational invariance techniques. IEEE Transactions on Acoustics Speech & Signal Processing, vol. 37, no. 7, pp. 984-995, July 1989.
[34] Ling H, Mqov J, Andevsh D J, Lee W and Hughes J. 3D scattering center representation of complex targets using the shooting and bouncing ray technique a review. IEEE Antennas and Wireless Propagation Letters, vol. 40, 1998.
[35] Freedman A, Bose R, Steinberg B D. Techniques to improve the CLEAN deconvolution algorithm[J]. Journal of the Franklin Institute, 1995, 332(5):535-553.
[36] Potter L C, Chiang D M, Carriere R and Michael J G, GTD Based Parametric Model for Radar Scattering, IEEE Transactions on Antennas and Propagation 43(1995), 1058-1067
[37] Dobre O A, Radoi E. Advances in subspace eigenanalysis based algorithms: from 1D toward 3D superresolution techniques. 5th International Conference on Telecommunications in Modern Satellite, Cable and Broadcasting Service. TELSIKS 2001. Proceedings of Thesis (Cat. No.01EX517), Nis, Yugoslavia, 2001, pp. 547-554 vol.2.
[38] Quinquis A, Radoi E and Totir F. Some radar imagery results using superresolution techniques. IEEE Transactions on Antennas and Propagation, vol. 52, no. 5, pp. 1230-1244, May 2004.
[39] Strobach P. Total least squares phased averaging and 3-D ESPRIT for joint azimuth-elevation-carrier estimation. IEEE Transactions on Signal Processing, vol. 49, pp. 54–62, Jan. 2001
[40] Schmidt R O. A Signal Subspace Approach to Multiple Emitter Location and Spectral Estimation[C]. Stanford University. 1981
[41] Ying B. Estimating Two-Dimensional Frequencies by Matrix Enhancement and Matrix Pencil, IEEE Transactions on Signal Processing 40(1992), 2267-2280
[42] Radoi E, Quinquis A and Totir F. Achieving superresolution by subspace

eigenanalys is in multidimensional spaces. 2002 11th European Signal Processing Conference, Toulouse, France, 2002, pp. 1-4.

[43] Wen X Y，Shi Z G，Zhao H Z, et al. A 3D-ESPRIT method for radar target scattering centers parameters estimation[J]. Radar Science and Technology, 2007，5(2) : 118-123

[44] Shin S Y, Lim H and H N. Myung. Estimating Three-Dimensional Scattering Centers of a Target using High Resolution Techniques[C]. 2007 Asia-Pacific Microwave Conference, 2007, pp. 1-4.

[45] Wang J, Zhou J J. An Extraction Method of target scattering center based on GTD Model[J]. Systems Engineering and Electronics, 2008(11):2146-2150.

[46] Akaike H. Information Theory and an Extension of the Maximum Likelihood Principle[C]. 2Nd International Symposium on Information Theory.1973, vol.73, pp.1033-1055.

[47] Akaike H T. A new look at the statistical model identification[J]. Automatic Control IEEE Transactions on, 1974, 19(6):716-723.

[48] Fishler E, Grosmann M and Messer H, Detection of signals by information theoretic criteria: general asymptotic performance analysis[J]. IEEE Transactions on Signal Processing, vol. 50, no. 5, pp. 1027-1036, May 2002.

[49] Rissanen J． Modeling by Shortest Data Description[J]. Automatica, 1978, 14(5)：465—471.

[50] Wax M, Ziskind I. Detection of the number of coherent signals by the MDL principle[J]. IEEE Transactions on Acoustics Speech & Signal Processing, 1989, 37(8):1190-1196.

[51] Wax M and Kailath T. Detection of signals by information theoretic criteria. IEEE Transactions on Acoustics Speech & Signal Processing, vol. 33, Feb. 1985.

[52] An Z J, Su H T, Bao Z. Source number estimation of spatial smoothing technique． Journal of Xi'an University of Science and Technology, 2008; 35(6) : 1009—1013.

[53] Reddy I S, Shevade S, Murty M N. A fast quasi-Newton method for semi-supervised SVM[J]. Pattern Recognition, 2011, 44(10-11):2305-2313.

[54] He Y, He S, Zhang Y, et al. A forward approach to establish parametric scattering center models for known complex radar targets applied to SAR ATR[J]. IEEE Transactions on Antennas and Propagation, 2014, 62(12): 6192-6205.

[55] Ding B Y. Research on target recognition method of synthetic aperture radar image

based on extended operating conditions[D]. National University of Defense Technology, 2018.
[56] Ding B, Wen G, Huang X, Ma C and Yang X. Target Recognition in Synthetic Aperture Radar Images via Matching of Attributed Scattering Centers. IEEE Journal of Selected Topics in Applied Earth Observations and Remote Sensing, vol. 10, no. 7, pp. 3334-3347, July 2017.
[57] Gonzalez R C, Woods R R. Digital Image Processing[M]. Princeton: Princeton-Hall, 2008.
[58] Gerry M J, Potter L C, Gupta I J, et al. A parametric model for synthetic aperture radar measurements[J]. IEEE Transactions on Antennas and Propagation, 1999, 47(7): 1179-1188.
[59] Koets M A, Moses R L. Feature extraction using attributed scattering center models on SAR imagery[C]. SPIE Algorithms for Synthetic Aperture Radar Imagery VI, 1999: 104-115.
[60] Potter L C, Moses R L. Attributed scattering centers for SAR ATR[J]. IEEE Transactions on Image Processing, 1997, 6(1): 79-91.
[61] Chiang H C, Moses R L, Potter L C. Model-based classification of radar images[J]. IEEE Transactions on Information Theory, 2000, 46(5): 1842-1854.
[62] Li D, Zhang G, Wu Z, et al. An Edge Embedded Marker-Based Watershed Algorithm for High Spatial Resolution Remote Sensing Image Segmentation[J]. Image Processing, IEEE Transactions on, 2010, 19(10):P.2781-2787.
[63] Li Y Y. Synthetic aperture Radar target recognition based on Convolutional Neural Network[D]. North University of China, 2020.
[64] Ryan M, William M, et al. Exploring characteristics of neural network architecture computation for enabling SAR ATR. Proc. SPIE 11729, Automatic Target Recognition XXXI, 1172909, April 2021.
[65] Krizhevsky A, Sutskever I, Hinton G. ImageNet Classification with Deep Convolutional Neural Networks[J]. Advances in neural information processing systems, 2012, 25(2).

Papers Published During Master's Studies

[1] **Y. R. Wang**, Y. M. Wu and X. Yi He, "3D Scattering Center Extraction Based on ESPRIT Algorithm," 2021 Cross Strait Radio Science and Wireless Technology Conference (CSRSWTC), 2021, pp. 269-271.

Acknowledgement

Time flies. At this moment, I have a lot of thoughts. But the most important thing is that I would like to express my sincere thanks to all the teachers, friends and relatives who have helped me.

I would like to express my sincere thanks to my tutors, Dr. Paavo Nevalainen, Assoc. prof. Tomi Westerlund and Prof. Yumao Wu. Since entering the master stage, Prof. Wu has taught me many things. Such as looking at problems from a global perspective and ignoring phenomena, paying attention to the physical nature of things, and jumping out of the trap of fixed patterns. These words gave me great inspiration, and thanks to the patient guidance of the professor.

I would like to thank Dr. Xinyi He of the Institute for her continuous care and help. During the research process, she gave a lot of selfless help, and it laid a solid foundation for the smooth progress of my project.

Thanks to my friends in the lab. When I encountered difficulties in study and life, they give me selfless help. They are talented and active in thinking. And each of them is an example for me to follow.

Thanks to my parents, their selfless dedication and unconditional love. They created a comfortable learning environment for me.